IFITM3 blocks viral entry by sorting lipids and stabilizing hemifusion

Steffen Klein,[1,6,7] Gonen Golani,[2,6,7] Fabio Lolicato,[3,4,7] Daniel Beyer,[3] Alexia Herrmann,[3] Moritz Wachsmuth-Melm,[1,6] Nina Reddmann,[1,6] Romy Brecht,[1,6] Carmen Lahr,[1,6] Mehdi Hosseinzadeh,[1] Androniki Kolovou,[1,6] Martin Schorb,[5] Yannick Schwab,[5] Britta Brügger,[3] Walter Nickel,[3] Ulrich S. Schwarz,[2,6] and Petr Chlanda[1,6,8,*]

[1] Schaller Research Group, Department of Infectious Diseases, Virology, Heidelberg University Hospital, 69120 Heidelberg, Germany.
[2] Institute for Theoretical Physics, Heidelberg University, 69120 Heidelberg, Germany.
[3] Biochemistry Center, Heidelberg University, 69120 Heidelberg, Germany.
[4] Department of Physics, University of Helsinki, Helsinki, Finland.
[5] Electron Microscopy Core Facility, European Molecular Biology Laboratory, 69117 Heidelberg, Germany.
[6] BioQuant-Centre for Quantitative Biology, Heidelberg University, 69120 Heidelberg, Germany.
[7] These authors contributed equally.
[8] Lead contact.
[*] Correspondence: chlanda@bioquant.uni-heidelberg.de

HIGHLIGHTS

- IFITM3 is localized in late endosomes and blocks viral membrane fusion
- IFITM3-induced lipid sorting can increase the energy barrier of viral fusion
- *In situ* cryo-ET confirmed hemifusion-stabilization as IFITM3's molecular mechanism
- IFITM3 does not interfere with conformational changes of the viral fusion machinery

SUMMARY

Interferon-induced transmembrane protein 3 (IFITM3) is a broad-spectrum restriction factor of viral entry, yet the molecular mechanism is poorly understood. We found that IFITM3 localizes to late endosomes, preventing viral fusion. Atomistic molecular dynamics simulations and continuum membrane modeling predicted IFITM3-induced local lipid sorting, resulting in an increased concentration of lipids disfavoring viral fusion at the hemifusion site. This increases the energy barrier of fusion pore formation and the hemifusion dwell time, promoting viral degradation in lysosomes. *In situ* cryo-electron tomography verified this model by visualizing influenza A virus-induced arrested membrane fusion at molecular resolution. Accumulated hemifusion diaphragms between viral particles and late endosomal membranes confirmed hemifusion stabilization as the molecular mechanism of IFITM3. The presence of hemagglutinin in post-fusion conformation close to hemifusion sites further showed that IFITM3 does not interfere with the viral fusion machinery, which corroborates IFITM3-induced lipid sorting as the primary cause of hemifusion stabilization.

KEYWORDS

IFITM3; Innate immunity; Viral entry; Membrane fusion; Lipid sorting; Influenza A virus; *In situ* cryo-ET; Subtomogram averaging; Molecular dynamics simulations; Continuum membrane modeling

GRAPHICAL ABSTRACT

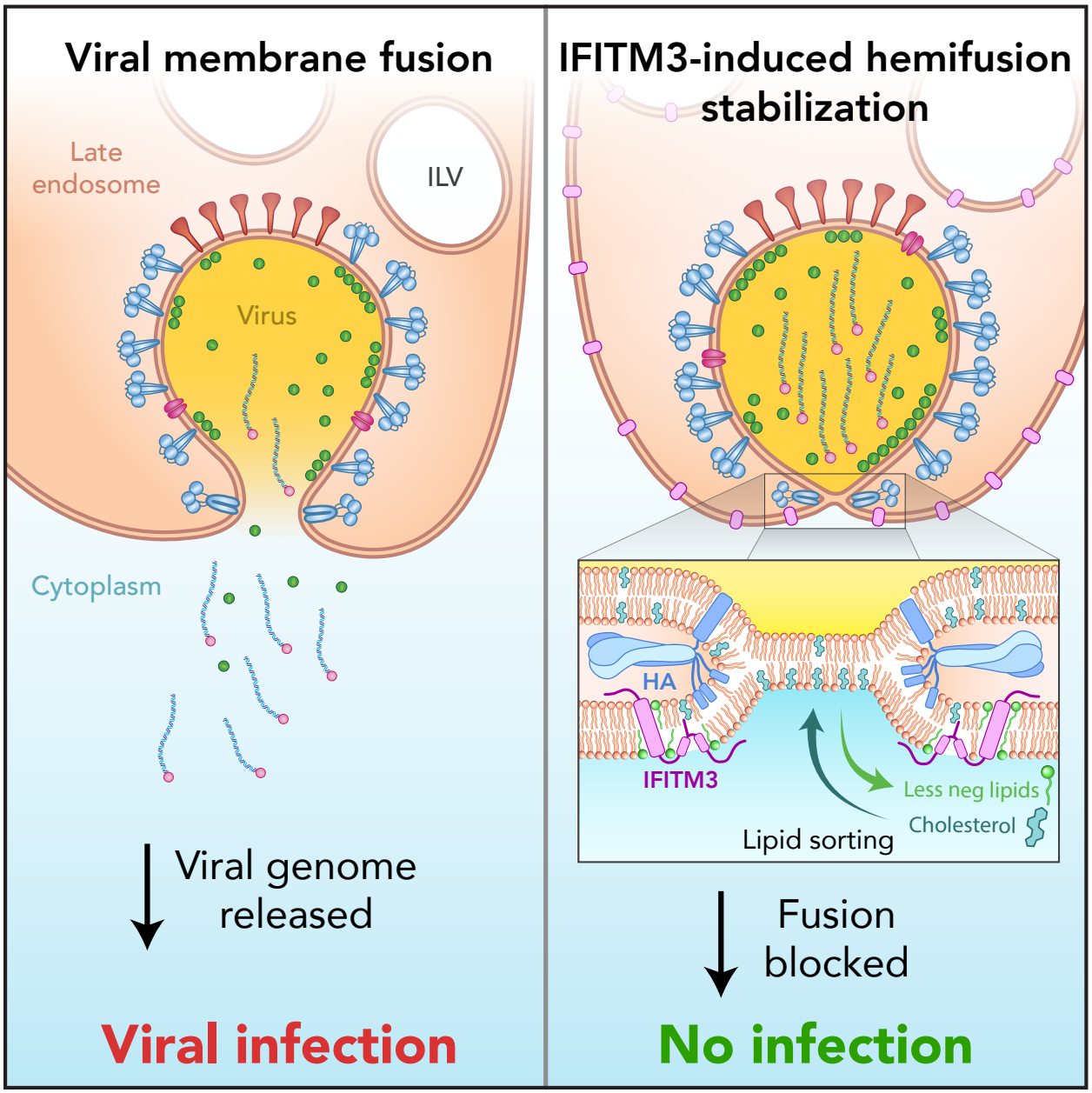

INTRODUCTION

Enveloped viruses such as influenza A virus (IAV) are the main cause of respiratory diseases. Maybe the most decisive step during infection is the release of the viral genome into the cytoplasm, for which viruses rely on their fusion machinery. Blocking this step is one of the most efficient countermeasures that the host cell can take. An infection by IAV starts with the virus attaching to the host cell by binding the trimeric surface glycoprotein hemagglutinin (HA) to sialic acid residues on the cell surface, followed by clathrin-mediated endocytosis (Matlin et al., 1981) or macropinocytosis (de Vries et al., 2011). The acidic environment in late endosomes, ranging between pH 5 and 6, induces complex conformational changes in the HA glycoprotein (Skehel et al., 1982) and triggers the disassembly of the viral matrix 1 (M1) layer. The trimeric pre-fusion HA structure undergoes extensive refolding with a loop to helix transition of the HA2 domain that leads to the formation of an extended HA intermediate (Benton et al., 2020; Bullough et al., 1994), which anchors the N-terminal fusion peptide into the late endosomal membrane. The extended intermediate folds back into an energetically more stable coiled-coil post-fusion state. The HA refolding provides the mechanical work required to overcome the repulsive hydration forces between the two opposing bilayers and bring them to proximity below 1 – 2 nm (Harrison, 2008). The viral and host proximal monolayers then merge to form a hemifusion stalk (Chen et al., 1999; Chernomordik et al., 2006; Kemble et al., 1994) which subsequently expands to a hemifusion diaphragm that brings the virus and hosts distal monolayers into contact along a joint mid-plane. The diaphragm is a mechanically stressed lipid structure, and transient membrane pores tend to open within it. This process is known as 'flickering pore' (Chanturiya et al., 1997; Frolov et al., 2000). The flickering pore undergoes open-close cycles due to thermal energy until it reaches a critical radius beyond which the pore tends to expand and complete the fusion (Chernomordik et al., 2006). The magnitude of the energy barrier for pore expansion depends on the lipid composition and determines the stability and dwell time of the hemifusion state. Fusion-pore opening is promoted by lipids with positive spontaneous curvature (e.g., lysophosphatidylcholine (LPC)) and inhibited by lipids with negative spontaneous curvature (e.g., cholesterol) in the virus and host distal monolayers (Chernomordik and Kozlov, 2003). While HA-mediated membrane fusion has been extensively studied *in vitro* and *in silico* (Fuhrmans et al., 2015), little is known about how this process is controlled in cells and how host cell restriction factors interfere with this process on the molecular level.

Interferon-induced transmembrane protein 3 (IFITM3) has evolved as a broad-spectrum cellular restriction factor that blocks cytosolic entry of IAV (Brass et al., 2009) and various

late penetrating viruses (Zani and Yount, 2018) by interfering with the fusion process. IFITM3 is a small (15 kDa) single domain transmembrane protein (Ling et al., 2016) localized in late endosomes (Feeley et al., 2011). It comprises two amphipathic helices facing the cytosolic side of the endosomal membrane, which are essential for its antiviral properties (Chesarino et al., 2017). IFITM3 is post-translationally modified by S-palmitoylation (Yount et al., 2010). In particular, palmitoylation at cysteine 72 (Cys72) was recently found to be essential for the functional incorporation of IFITM3 into the endosomal membrane (Garst et al., 2021). Fluorescence microscopy-based live-cell imaging revealed that while IFITM3 effectively blocks the release of the viral genome into the cytoplasm, lipid mixing between the viral and endosomal membrane could still be observed (Desai et al., 2014). Based on these data, two alternative models were proposed. In the so-called 'hemifusion stabilization' model, IFITM3 interferes with the fusion pore formation in a direct or indirect mode of action, whereas, in the 'fusion decoy' model, IFITM3 increases the number of endosomal intraluminal vesicles (ILVs) which may serve as a decoy target for virus membrane fusion (Desai et al., 2014). *In vitro* experiments suggest that IFITM3 may function by altering the biophysical properties of the membrane (Guo et al., 2021) or by changing the lipid composition and cholesterol levels of the endosomal membranes (Amini-Bavil-Olyaee et al., 2013; Das et al., 2021; Kühnl et al., 2018). Despite many studies on IFITM3, the exact mode of action remains to be clarified and has not yet been addressed on the molecular level and directly inside the infected host cells.

In this study, we first characterized the morphology of IFITM3-containing endosomes and utilized atomistic molecular dynamics simulations to understand the interaction of IFITM3 with specific lipids. Continuum membrane modeling further allowed us to reveal lipid sorting as the primary molecular mechanism underlying the antiviral properties of IFITM3 by increasing the energy barrier of fusion pore formation. Finally, *in situ* cryo-electron tomography (cryo-ET) was applied to test this hypothesis experimentally and structurally characterize stabilized hemifusion sites in late endosomes at molecular resolution in the native cellular environment.

RESULTS & DISCUSSION

IFITM3 does not alter the number of intraluminal vesicles in the late endosomal lumen

While IFITM3 expression can be induced by interferon-beta (IFNβ) in a concentration-dependent manner, interferon treatment leads to the induction of additional restriction factors that may inhibit viral entry. To study the antiviral effect of IFITM3, human epithelial lung cells A549 stably overexpressing non-tagged IFITM3 (A549-IFITM3) were established and characterized. The A549-IFITM3 cell line showed a significant 3.9–fold increase in IFITM3 expression level compared to A549 cells induced with 2×10^3 units/ml IFNβ (Figure 1A, Figure S1A and S1B). Confocal microscopy was performed to assess the density and volume of IFITM3-positive organelles. As expected, both IFNβ treatment and stable IFITM3 expression increased the number of IFITM3-positive cellular organelles in A549 cells (Figure 1B–H). Three-dimensional segmentation (Figure 1C, 1E, and 1G) revealed a 3.1–fold increase in the number of organelles (Figure 1H) and a moderate but significant 1.3–fold increase in average organelle volume of 0.39 μm^3 (SD = 0.41 μm^3, n = 2,402) (Figure S1C) when compared to the IFNβ treated A549 cell line. As IFITM3 localizes to late endosomes (Feeley et al., 2011), our data indicate that IFITM3 expression changes the size of late endosomes. To characterize the antiviral effect of the A549-IFITM3 cell line, cells were infected with a reporter influenza virus A/WSN/1933 carrying PA-mScarlet (Bindels et al., 2016), immunolabelled against M2, and subjected to high-throughput, automated fluorescent microscopy (Figure 1I–P). While A549 cells showed an infection rate of 98.8 % (n = 1,136) (Figure 1O), the infection rate in A549-IFITM3 was dramatically decreased (11.5–fold) as only 8.2% (n = 2,009) of the cells were infected (Figure 1P). These data agree with the previously reported antiviral properties of IFITM3 (Brass et al., 2009). To further validate the antiviral properties of the A549-IFITM3 cell line, we performed a β-lactamase (Blam) cell entry assay utilizing influenza A virus-like particles (VLPs) expressing M1-Blam (Tscherne et al., 2010). Our data show an IFNβ concentration-dependent decrease in relative viral entry with an up to 8.7–fold decrease. In comparison, A549-IFITM3 showed a relative viral entry inhibition of 10.7–fold (Figure 1Q and Figure S1H). This data is consistent with previous studies (Desai et al., 2014; Feeley et al., 2011), indicating that viral-induced membrane fusion in late endosomes is inhibited and validates that the here established A549-IFITM3 cell line effectively blocks viral cytoplasmic entry by IFITM3 overexpression.

As IFITM3 expression increases the volume of late endosomes (Figure 1B–H), we further analyzed the impact of IFITM3 expression on the late endosomal morphology. IFITM3-induced alterations of the late endosomal morphology were previously proposed as an IFITM3 inhibitory mechanism in the 'fusion decoy' hypothesis (Desai et al., 2014), where an increased number of ILVs in the late endosomal lumen might diverge the site of membrane fusion. To determine morphological changes of late endosomes in the presence of IFITM3, electron tomography (ET) of high-pressure frozen and freeze-substituted (HPF/FS) A549-IFITM3 cells was performed (Figure 1R–Y). As the 'fusion decoy' hypothesis suggested an increase in ILVs, we analyzed late endosomes in a total of 77 tomograms of A549 cells (n = 19), A549 cells treated with 2×10^3 units/ml IFNβ (n = 34), and A549-IFITM3 cells (n = 24). The endosomal membrane and individual ILVs were segmented in three dimensions for each tomogram (Figure1S, 1U, 1W) to quantify the endosomal volume (Figure S1I). Consistent with confocal microscopy data (Figure S1C), a modest but significant 1.6–fold increased late endosomal volume in A549-IFITM3 cells compared to non-treated A549 cells was determined (Figure S1I). Immuno-gold-labeling against IFITM3 showed that late endosomes in A549-IFITM3 cells displayed a significantly higher (5.3–fold) IFITM3 labeling than A549 cells (Figure 1X and Figure S2). This data is consistent with the increased IFITM3 expression levels of A549-IFITM3 cells (Figure 1A) and shows that IFITM3 is specifically localized to late endosomes featuring a characteristic multivesicular morphology. Importantly, our data revealed no significant difference in the number of ILVs per endosome between A549 cells, IFNβ-treated A549 cells, or A549-IFITM3 cells (Figure 1Y).

Overall, these findings show that IFITM3 localizes to late endosomes with multivesicular morphology. However, IFITM3 expression is not affecting the number of ILVs in late endosomes, contradicting the assumptions of the 'fusion decoy' model.

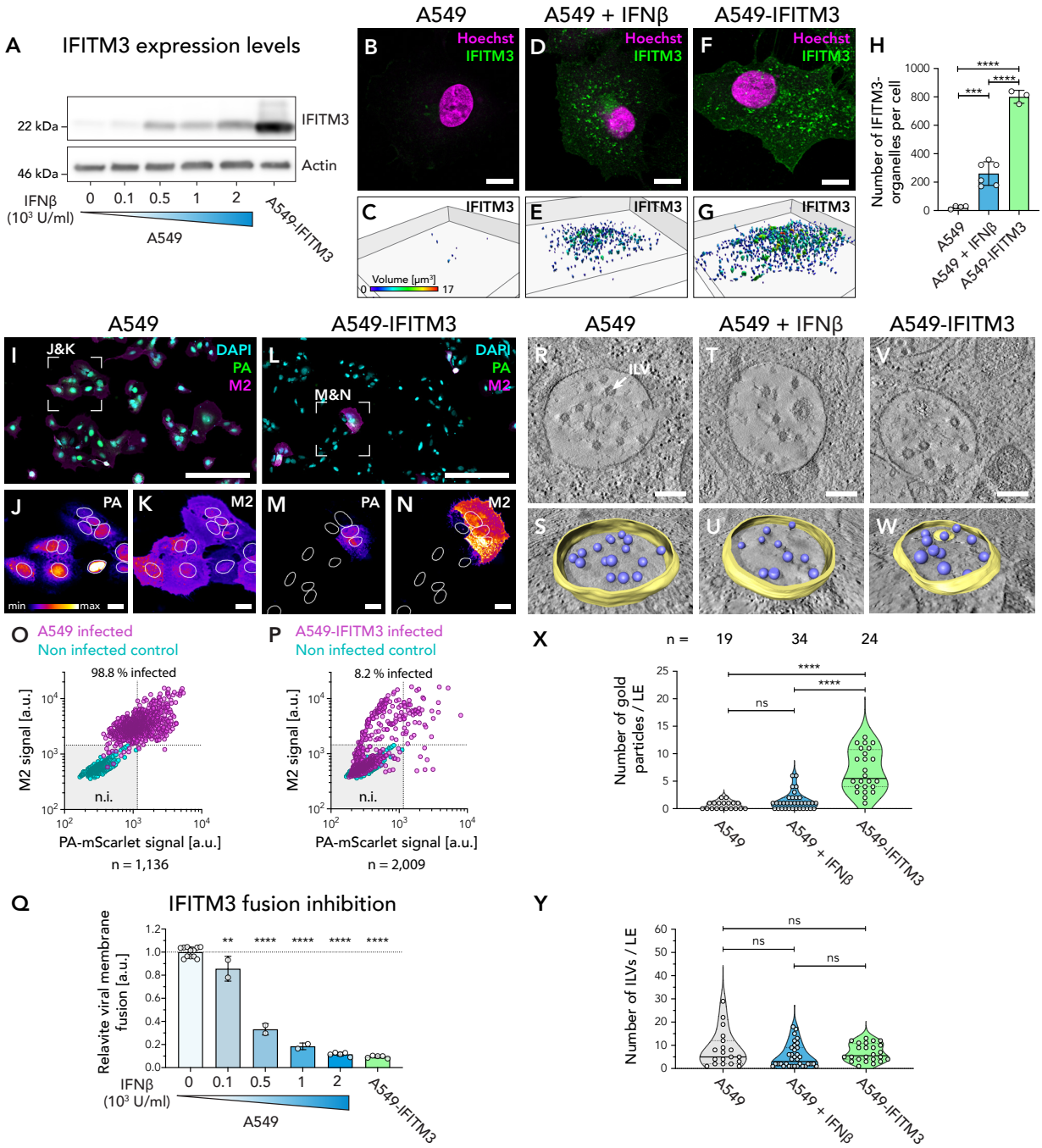

Figure 1. IFITM3 inhibits IAV infection by blocking viral membrane fusion without altering the number of ILVs in the late endosomal lumen. (A) Immunoblot analysis of A549 cells treated with increasing IFNβ concentrations and A549-IFITM3 cells. The cell lysate was analyzed by western blotting and immunolabeling against IFITM3. Actin was used as a loading control. See Figure S1A for quantification of expression levels and Figure S1B for the full image of the blot. **(B–G)** Confocal fluorescence microscopy analysis of A549 cells (B, C), A549 cells treated with 1 × 10^3 units/ml IFNβ (D, E), and A549-IFITM3 cells (F, G). Cells were immunolabeled against IFITM3 (shown in green), and the nucleus was stained with Hoechst 33342 (shown in magenta). The top row (B, D, F) shows

a composite central slice of a representative cell. The bottom row (C, E, G) shows the three-dimensional segmentation of the IFITM3 signal. Individual objects are color-labeled according to their volume. The outer limits of the image volume are indicated. **(H)** The number of individual IFITM3 organelles per cell, as quantified by three-dimensional IFITM3 signal segmentation (C, E, G). Each data point represents the quantification of an individual cell. The bar graph shows the mean value with standard deviation (SD). An unpaired t-test was performed to evaluate the significance of differences between samples. **(I–N)** IAV infection assay for A549 cells (I–K) and A549-IFITM3 cells (L–N). Cells were infected with the fluorescent reporter virus A/WSN/1933-PA-mScarlet (MOI = 3) (shown in green) and fixed 24 hours post-infection (hpi). The viral protein M2 (shown in magenta) was labeled by immunofluorescence staining, and nuclei were labeled with DAPI (shown in cyan). Composite overview images for both conditions are shown (I and L). For each condition, a magnified area (indicated as white squares) for the signals of PA-mScarlet and M2 are shown in the bottom row (J, K, M, N) using a fire lookup table. Individual nuclei were segmented (indicated with white outlines), allowing for measuring the average signal intensity for PA-mScarlet and M2 in the segmented area. **(O and P)** Quantification of infection rate for A549 cells (O) and A549-IFITM3 cells (P). For each segmented nucleus, the signal intensity for PA-mScarlet and M2 is shown as a scatter blot for infected cells (magenta) and non-infected control (cyan). Two thresholds of M1 ≤ 1,150 a.u. and PA-mScarlet ≤ 1,450 a.u. (dotted lines) were defined for non-infected (n.i.) cells (shown as a grey square), and accordingly, all other cells are defined as infected. See Figure S1D–G for immunofluorescence images and scatter plots of the non-infected control only. **(Q)** Blam-based cell entry assay for A549 cells treated with increasing IFNβ concentrations and A549-IFITM3 infected with M1-Blam influenza A VLPs. Signal for non-cleaved and cleaved FRET-biosensor was measured in bulk using a plate reader, and the normalized ratio was determined. Each data point represents a biological replicate. An unpaired t-test was performed to evaluate the significance of differences for all samples compared to non-treated A549 cells. See Figure S1H for fluorescence microscopy images of all samples. **(R, T, V)** Tomographic slices of A549 cells (R), A549 cells treated with 2×10^3 units/ml IFNβ (T), and A549-IFITM3 cells (V). A representative late endosome was selected for each sample with the typical multivesicular morphology, characterized by ILVs in the late endosomal lumen. One ILV is indicated (white arrow in R). To increase contrast, 10 slices were averaged (10.9 nm), and a low pass filter (3.09 nm) was applied. See Figure S2 for a gallery of late endosomes for each condition. **(S, U, W)** Three-dimensional segmentation of the late endosomes is shown in (R, T, V). The late endosomal membrane (yellow) and individual ILVs (purple) were manually segmented. **(X)** Quantification of anti-IFITM3 immunogold particles per late endosome. See Figure S2 for a gallery of immuno-gold-labeled late endosomes. **(Y)** Quantification of the number of ILVs per endosome. Statistical significance: * for $p < 0.05$, ** for $p < 0.01$, *** for $p < 0.001$ **** for $p < 0.0001$. Scale bars: (B–F) 10 µm, (I & L) 200 µm, (J, K, M, N) 20 µm, (R, T, V) 200 nm.

IFITM3 modulates the local lipid composition of the endosomal membrane

As electron tomography revealed that IFITM3 does not modulate the overall morphology of late endosomes (Figure 1R–Y), we next analyzed the impact of IFITM3 on the lipid composition of these organelles. It has been previously reported that IFITM3 alters the cholesterol level in endosomes (Amini-Bavil-Olyaee et al., 2013). To determine whether IFITM3 directly interacts with cholesterol, we performed UV cross-linking using a photo-reactive and clickable cholesterol analog (pacChol) as a probe to map cholesterol-IFITM3 interactions directly in

living cells. Western blot analysis of immunoprecipitated pacChol showed that IFITM3 and cholesterol directly interact (Figure 2A), as suggested recently (Das et al., 2021).

To further characterize the IFITM3-cholesterol interaction, we employed atomistic molecular dynamics (MD) simulations of IFITM3 embedded in different lipid compositions. The used MD systems have a box size of 8.5 x 8.5 x 8.9 nm, and were simulated in triplicate for a cumulative time of 3 microseconds using the CHARMM36m force field (Huang and MacKerell, 2013; Huang et al., 2017; Pastor and Mackerell, 2011). As palmitoylated Cys72 is essential for IFITM3s antiviral properties (Garst et al., 2021), this modification was incorporated in all MD simulations. First, we analyzed the contact occupancy for each amino acid of IFITM3 in a binary POPC–cholesterol (90:10) model membrane (Figure 2B). Our data revealed that while most IFITM3 amino acids showed a low probability of interactions with cholesterol, there is an increased interaction probability in the cytosolic region of the transmembrane domain (Figure 2C). In addition to this transmembrane section, our analysis revealed that the palmitoylated Cys72 displayed the strongest cholesterol-interaction probability of 1.9×10^{-2} (SD = 1.3×10^{-3}, n = 3) (Figure 2C), which highlights the importance of this post-translationally modification. Next, we investigated the IFITM3-cholesterol interactions in a complex membrane environment by simulating IFITM3 in a late endosomal-like membrane (Kobayashi et al., 2002; Van Meer et al., 2008) composed of eight different lipids. The IFITM3–lipid interaction landscape was investigated by comparing the molar fraction of lipids surrounding IFITM3 with the lipid bulk concentrations at a radial distance of 0.4 nm around IFITM3 (Figure 2D, green lipids). The enrichment and depletion analysis showed that IFITM3 modulates lipid distribution in its vicinity. Our data highlight a statistically significant ($p = 0.003$, Figure S3C) depletion of cholesterol from the vicinity of IFITM3 by 10.8% (SD = 2.7%, n = 3) (Figure 2E). The repelled cholesterol is mainly replaced by POPC (Figure 2E), which shows a statistically significant ($p = 0.023$, Figure S3C) enrichment of 8.4% (SD = 3.9%, n = 3) in IFITM3s vicinity. To understand if the cholesterol levels in the membrane influence this IFITM3-induced lipid-sorting, we analyzed binary POPC–cholesterol lipid systems at cholesterol concentrations of 10, 20, and 30 mol%. We found that the IFITM3-induced cholesterol depletion activity can be observed in all tested cholesterol concentrations in a linear concentration-dependent manner (Figure 2F). To further analyze whether the observed IFITM3-induced cholesterol depletion effect is due to cholesterol's intrinsic negative curvature, we utilized two ternary lipid systems. In a POPC–cholesterol–LPC (80:10:5) system, we observed a similar cholesterol depletion effect as shown in all other systems (Figure 2G). Next, we replaced cholesterol in this system with DOPE, a lipid with an intrinsic negative

curvature comparable to cholesterol. Surprisingly, in contrast to cholesterol, DOPE is not depleted in the IFITM3 vicinity (Figure 2H), suggesting that the IFITM3-mediated cholesterol depletion activity is not dependent on the intrinsic curvature of the lipid but rather cholesterol specific. Finally, we calculated the relative repulsion energy of cholesterol from IFITM3 compared to all of the other lipids in the system based on the de-mixing entropy of cholesterol depletion near IFITM3 (Figure 2D, green lipids) and its accumulation in bulk (Figure 2D, orange lipids). We found the repulsion strength in the endosomal-like lipid composition to be 0.7 k_BT (SD = 0.2 k_BT, n = 3). Repulsions calculated from membrane models with different lipid compositions were similar (Figure 2I), indicating that the repulsion is independent of the cholesterol concentration.

In conclusion, our MD results emphasize a dual nature of the IFITM3-cholesterol interaction. On the one hand, we observed selective cholesterol binding to the transmembrane domain and the palmitoylated Cys72, which might be important for specific localization of IFITM3 to cholesterol-rich late endosomal membranes. On the other hand, the local cholesterol repulsion ability of IFTM3 leads to local lipid sorting in the late endosomal membrane.

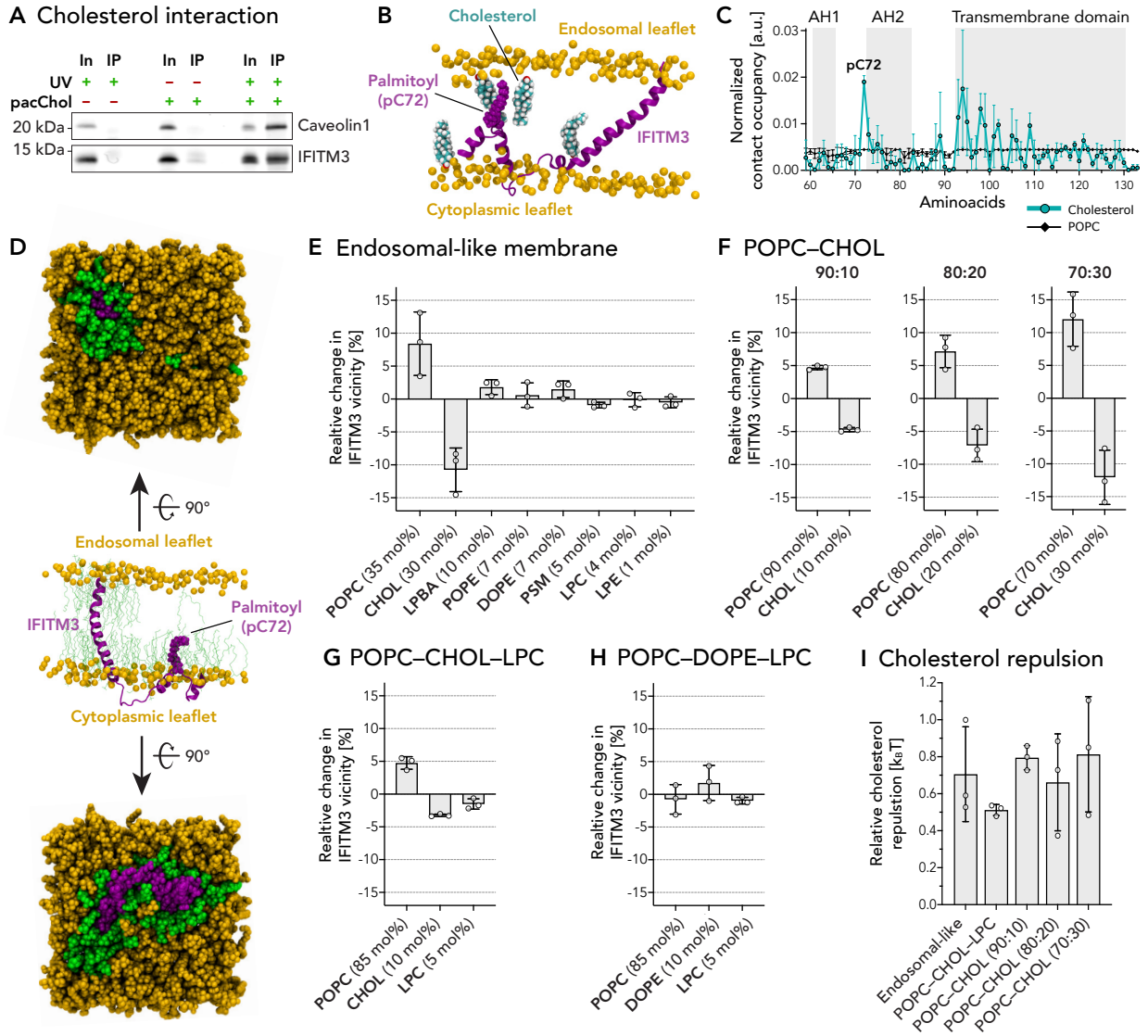

Figure 2. Molecular dynamics simulations predict IFITM3-induced lipid sorting by selective lipid binding. **(A)** Analysis of IFIMT3-cholesterol interactions in A549-IFITM3 cells. Cells were treated with a photo-reactive and clickable cholesterol analog (pacChol). After UV cross-linking and immupoprecipitation (IP), immunoblot analysis was performed against IFITM3. Caveolin1 was used a positive control, as it is known to interact with cholesterol (de Marco et al., 2001). Complete cell lysate input (In) and immunoprecipitated samples (IP) were analyzed for conditions treated with UV and/or pacChol. Fulls blots can be found in Figure S3A and S3B. **(B)** Representative snapshot of the interaction between cholesterol molecules and IFITM3 in a binary POPC–cholesterol (90:10) system. IFITM3 is represented as ribbon (magenta), the palmitoyl group of Cys72 is represented as atom sphere model, having a van der Waals (vdW) radius of their respective atoms. Phosphorus atoms of the POPC head groups are represented as atom sphere model (orange). POPC tails are not shown. Cholesterol molecules in contact (distance < 0.4 nm) with IFITM3 are represented as atom sphere model (cyan), with oxygen atom in red and hydrogen atoms in white. Non-interacting cholesterol molecules are not shown. **(C)** Normalized contact occupancy between IFITM3 and POPC (black graph) or cholesterol (cyan graph) in a binary POPC–cholesterol (90:10) model membrane as shown in (B). A contact

is defined if the distance between any atoms of IFITM3 and POPC (or cholesterol) is less than 0.4 nm. Data are normalized based on the total number of lipid of each lipid type. The sequence sections for the two amphipathic helix domains (AH1 and AH2) and the transmembrane domain are indicated. Error bars are shown as standard deviation (SD). **(D)** A representative snapshot of IFITM3 (magenta), with palmitoylated Cys72, embedded in a late endosomal-like model membrane (orange). The central side view shows IFITM3 as ribbon model, with the palmitoyl-group at Cys72 as atom sphere model. Lipid tails of lipids in close vicinity to IFITM3 (< 0.4 nm) are shown as stick model (green), all other lipid tails are hidden. The top views of both the endosomal (top) and cytoplasmic (bottom) leaflets are shown. All molecules are shown as atom sphere model, with IFITM3 in magenta, lipids in close vicinity to IFITM3 (< 0.4 nm) in green and all other lipids in orange. **(E–H)** Relative changes of lipid concentrations in the vicinity of IFITM3 (< 0.4 nm) for different lipid systems: Late-endosomal like lipid system (E); binary POPC–cholesterol lipid system with cholesterol concentrations of 10, 20, and 30 mol% IFITM3; ternary POPC–cholesterol–LPC lipid system (G); and ternary POPC–DOPE–LPC lipid system. **(I)** Cholesterol repulsion from IFITM3 for all studied membrane systems. All plots in (E–I) show the mean of three independent MD simulation runs. Individual values are indicated. The error bar represents the standard deviation (SD).

IFITM3-induced lipid sorting increases the energy barrier for fusion pore formation

Previous experimental studies suggested that IFITM3 blocks membrane fusion pore formation (Desai et al., 2014; Guo et al., 2021; Suddala et al., 2019). However, the mechanism facilitating this inhibition remained unknown. We suggest that the observed cholesterol repulsion from the IFITM3 vicinity (Figure 2E-I) and its accumulation in the virus and hemifusion diaphragm membranes are the primary force behind the fusion inhibition. The hemifusion diaphragm rim is a three-way junction between the endosomal and viral membranes (Figure 3A). It is characterized by a strong lipid tilt and splay that decays at a 3 – 4 nm distance from the rim (Akimov et al., 2020; Golani et al., 2021; Kozlovsky et al., 2002). As a result, the transmembrane domain of IFITM3 is repelled from it and cannot pass the rim to the diaphragm and virus membranes (Figure 3A, TM domain repulsion region). Since the amphipathic helices and the Cys72 domains of IFITM3 span about 2.5 nm from the transmembrane domain (Figure 3A), it is unlikely that any part of the IFITM3 protein can reach the diaphragm. In such a setting, the hemifusion diaphragm rim and its surroundings act as a semipermeable barrier between the compartments, allowing only lipids to pass but not IFITM3. As a result of IFITM3-induced cholesterol repulsion, cholesterol is likely to be enriched in IFITM3-free regions of the hemifusion diaphragm and virus membranes and be replaced by more positively curved lipids (Figures 3B), causing local lipid-sorting. Thus, the mean intrinsic curvature of the hemifusion diaphragm monolayers should shift to more negative values. This shift leads to a decrease in mechanical stress in the diaphragm (Akimov et al., 2020; Golani et al., 2021; Kasson and Pande, 2007) and an increase in membrane pore

line tension (Chernomordik et al., 1995; Lee, 2010; Portet and Dimova, 2010), which in turn increases the energy barrier of fusion pore expansion and inhibits fusion.

To test this hypothesis, we used the theory of membrane elasticity (Figure 3C) (Hamm and Kozlov, 2000; Helfrich, 1973) and continuum modeling of the fusion site (Akimov et al., 2020; Golani et al., 2021; Kozlovsky et al., 2002) to calculate the mechanical stress and energy barrier of membrane fusion pore expansion. We took the relative repulsion between cholesterol and IFITM3 as the 'late endosome membrane' composition of 0.7 k_BT as derived from the MD simulations (Figure 2I) and determined the lipid sorting between the endosome and diaphragm membrane as a function of the IFITM3 mole fraction. We found that cholesterol is enriched in hemifusion diaphragms at a rate of 7.0%/(mol_{IFITM3} %) beyond the baseline value of 30%, leading to the reduction of the monolayer spontaneous-curvature by 0.027 nm^{-1}/(mol_{IFITM3} %) (Figure S4A), and an increase of membrane-pore rim line tension by 4.96 pN/(mol_{IFITM3} %) (Figure S4A). Next, we simulated the fusion site shape (Figure S4B) and the stress in the diaphragm as a function of the IFITM3 mole fraction (Figure S4C). Based on the tilt and splay deformations, we calculated the decrease in mean mechanical stress in the diaphragm to be 0.21 $k_BT/(nm^2 \cdot mol_{IFITM3}$ %) (Figure 3D). Due to IFITM3-induced cholesterol sorting, which resulted in a decrease in stress and increased line tension, the energy barrier (Figure 3E) for flickering pore expansion increased by 17 $k_BT/(mol_{IFITM3}$ %) (Figure 3F, sensitivity to cholesterol-IFITM3 relative repulsion presented in Figure S4D). Hence, IFITM3 can inhibit fusion pore expansion due to the IFITM3-cholesterol sorting effect.

A recent study reported that the amphipathic helix domain of IFITM3 induces strong negative membrane curvature (Guo et al., 2021), which may influence the outcome of membrane fusion in addition to lipid sorting. Thus, we next calculated the changes in mean mechanical stress and energy barrier of fusion pore expansion when IFITM3-induced negative membrane curvature was considered alone or combined with IFITM3-induced lipid sorting. Overall, IFITM3-induced negative curvature slightly increased the energy barrier of fusion pore expansion in the presence of lipid sorting (from 17 to 18 $k_BT/(mol_{IFITM3}$ %) (Figure 3F). However, in the absence of lipid sorting, the energy barrier decreased by 4.4 $k_BT/(mol_{IFITM3}$ %)) (Figure 3F), accelerating fusion. We also tested the possibility that the amphipathic helix domain of IFITM3 penetrates the diaphragm with no lipid sorting. In such a case, the fusion-pore formation energy barrier increases only by 0.45 $k_BT/(mol_{IFITM3}$ %). Hence, our findings show that IFITM3-induced lipid sorting is the main effector of fusion pore expansion inhibition. This important lipid sorting activity of IFITM3 might be partially caused by the ability of IFITM3 to induce negative membrane curvature (Guo et al., 2021).

As IFITM3 increases the energy barrier of fusion pore expansion, the time required to complete viral membrane fusion in late endosomes, hereafter termed 'dwell time', increases. We quantified this increase by calculating the ratio between the dwell time in the presence of IFITM3, τ_{IFITM3}, to the dwell time without IFITM3, τ_0 (Figure 3G). Our data showed that even a modest concentration of 0.16% IFITM3 (one IFITM3 molecule per 625 lipids) increases the dwell time by a factor of 14 if we consider both the sorting and direct mechanical effect of IFITM3. In summary, continuum membrane modeling results predict that IFITM3-induced lipid sorting leads to an increased energy barrier for fusion pore formation and thus to a prolonged dwell time of fusion pore formation.

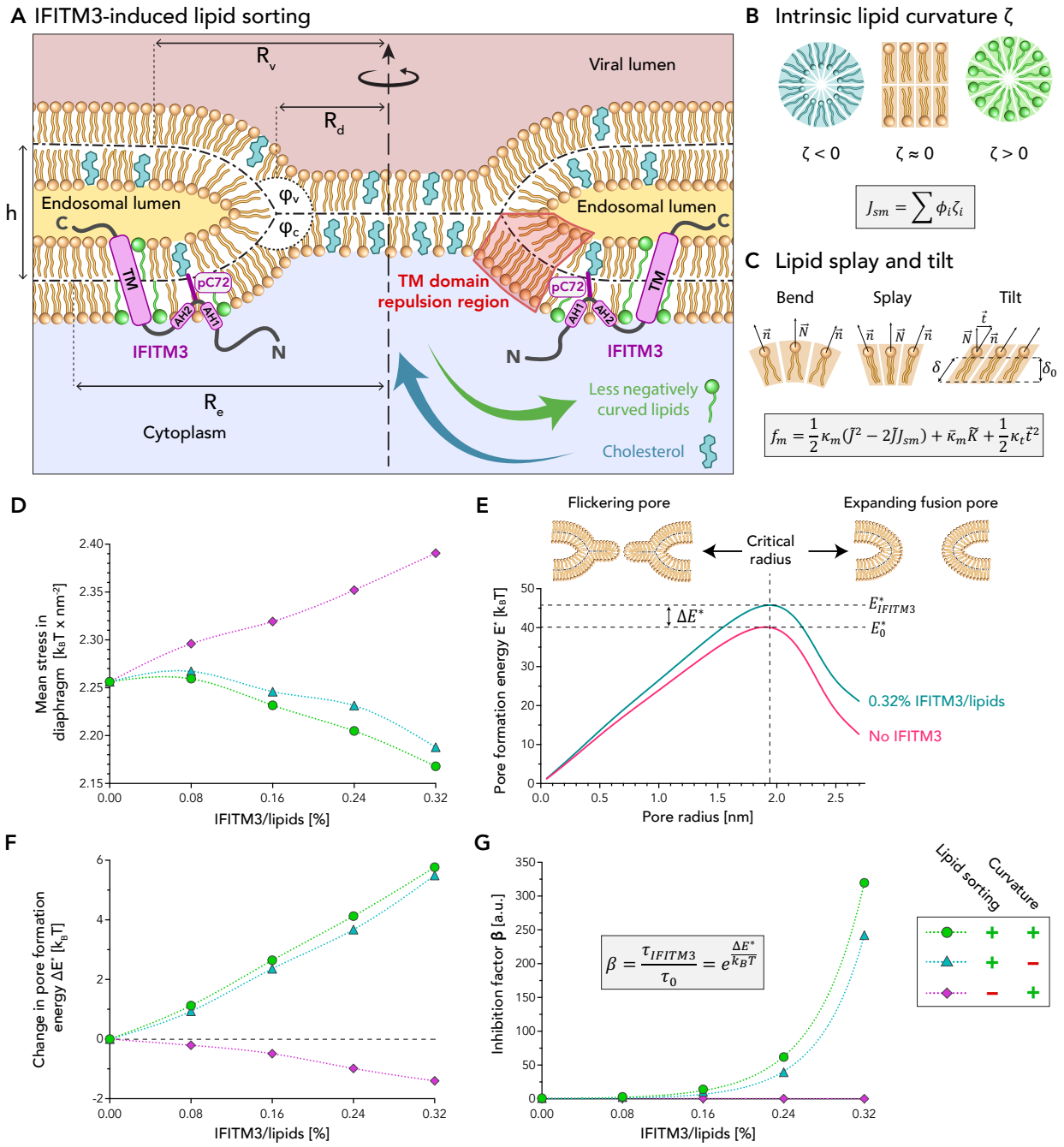

Figure 3. Continuum membrane modeling predicts that IFITM3-induced lipid sorting increases the energy barrier for fusion pore formation and thus stabilizes the hemifusion state. **(A)** Schematic representation of a hemifusion diaphragm during viral membrane fusion at the late endosome. The viral lumen (red), endosomal lumen (yellow), and cytoplasmic lumen (blue) are indicated. The geometry of the fusion site is defined by: The hemifusion diaphragm radius, R_d; the distance between the mid-planes of fusing membranes, h; and the inner angles in the cytosol and virus lumen side, φ_c and φ_v, respectively. The radii of the fusion site, R_v and R_e, are defined as the distance from the center to where tilt and splay deformation vanish. The geometry of the fusion site is not fixed and is subjected to energy minimization. The main structural features of IFITM3 are shown in purple: The transmembrane

domain (TM), the two amphipathic helixes (AH1 and AH2) as well as the palmitoylated cystin 72 (pC72), which interacts with a cholesterol molecule. The 'TM domain repulsion region' (dark red) represents the area near the diaphragm rim with a very strong tilt and splay. The TM domain of the IFITM3 is repelled from this region. IFITM3-induced lipid sorting is indicated with the blue and green arrows: IFITM3 repels negatively curved cholesterol from its vicinity. As a result, less negatively curved lipids (e.g., POPC) are accumulated in the vicinity of IFITM3, which leads to a decreased concentration of these lipids at the hemifusion diaphragm. **(B)** Schematic models of different intrinsic lipid curvatures, ζ_i. The monolayer spontaneous-curvature, J_{sm}, is the averaged sum of all the lipid components with ϕ_i being the mole fraction of each component (Equation 5, STAR★METHODS). **(C)** Theory of lipid splay-tilt and lipid monolayer energy density, f_m (Equation 4, STAR★METHODS). Schematic representations of lipid bend, splay, and tilt are shown, with the lipid director, $\vec{n}$; the normal to the mid-plane director , $\vec{N}$; the lipid tilt director, $\vec{t}$; the length of lipid tails, δ; and relaxed lipid tail length, δ_0. Monolayer bending rigidity, κ_m; lipid splay, $\tilde{J}$; monolayer spontaneous-curvature, J_{sm}; monolayer saddle-splay modulus, $\bar{\kappa}_m$; lipid saddle-splay, $\tilde{K}$; tilt modulus, κ_t. **(D–G)** Results of the continuous membrane modeling. The following parameters were used in all simulations: $\kappa_m = 14.4\,\mathrm{k_BT}$, $\bar{\kappa}_m = -7.2\,\mathrm{k_BT}$, $\kappa_t = 40\,\mathrm{mN/m}$, $\delta_0 = 1.5\,\mathrm{nm}$, $\zeta_{chol} = -0.5\,\mathrm{nm^{-1}}$, $\zeta_0 = -0.1\mathrm{nm^{-1}}$, $\phi_{chol} = 0.3$ and $\lambda_0 = 15\,\mathrm{pN}$. The lipid distribution scenarios used in (D, F, and G) are indicated in the legend. **(D)** Mean stress due to splay and tilt deformations in the diaphragm as a function of IFITM3 concentration. **(E)** Pore formation energy, E^*, as a function of the pore radius in a model without IFITM3 (magenta graph) and with a 0.32% IFITM3/lipid ratio (blue-green graph). The 'with sorting; with curvature' scenario was used here. The critical radius represents the transition from flickering pore to expanding fusion pore. **(F)** Change in fusion-pore formation energy, $\Delta E^* = E^*(\phi_{IFITM3}) - E_0^*$, as a function of IFITM3 concentration, with E_0^* being the energy barrier without IFITM3 and $E^*(\phi_{IFITM3})$ being the energy barrier with the IFITM3 mole fraction, ϕ_{IFITM3}. **(G)** Inhibition factor, β, of IFITM3 (Equation 18, STAR★METHODS), which describes the ratio between the time of pore opening with IFITM3, τ_{IFITM3}, and without IFITM3, τ_0, as a function of IFITM3 concentration.

IFITM3 stabilizes the hemifusion state in late endosomes

As atomistic MD-simulation and continuum membrane modeling suggest that IFITM3 increases the energy barrier of fusion pore formation and thus the dwell time, viral-induced membrane fusion in late endosomes should be arrested in the hemifusion state. To validate this theoretical model, we utilized *in situ* cryo-ET, which allows direct visualization of membrane-protein interactions inside cells in native conditions. We fluorescently labeled the viral membrane of influenza A virus particles using a lipophilic dye to localize late endosomes with trapped viral particles. A549-IFITM3 cells were infected with this fluorescently labeled virus and were plunge frozen one hour post-infection (hpi). Using *in situ* cryo-correlative light and electron microscopy (cryo-CLEM) (Klein et al., 2021a), infected cells were selected for cryo-focused ion beam (cryo-FIB) milling to prepare cryo-lamellae (Marko et al., 2007; Rigort et al., 2012). Cryo-EM of lamellae showed putative endosome-like organelles that were used as sites for tomography acquisition, and subsequent correlation allowed us to validate the presence of labeled virions in these endosomal compartments (Figure 4A–D and Figure S5). Cryo-ET revealed the ultrastructure of late endosomes (Figure 4E and 4F, Video S1) with a

similar multivesicular structure as observed by ET (Figure 1V), showing protein-coated ILVs (Figure S6). In addition to ILVs, we observed a total of 43 individual viral particles in late endosomes and early lysosomes of four different cells (Figure 4E, Figure S7–S9, Videos S1–S4), indicating that these viruses are unable to enter the cytoplasm, as IAV membrane fusion should occur within 10 minutes after entry in the absence of IFITM3 (Dou et al., 2018).

Viral particles showed a characteristic diameter of 87.8 nm (SD = 7.8 nm, n = 18). Intriguingly, IAV particles were regularly bound to small crystal-like structures (Figure 4I and 4L, arrowheads), which are structurally similar to low-density lipoprotein particles containing a cholesterol ester core (Kumar et al., 2011) and to structures found in late endosomes and lysosomes (Klein et al., 2021b). All viral particles featured a distinct disorganized HA glycoprotein phenotype comparable to *in vitro* cryo-ET studies of IAV particles at pH 4.9 (Fontana et al., 2012). The M1 matrix layer was partially disassembled in 83% of the observed viral particles and fully disassembled in 9%. The remaining 8% of viral particles did not show any sign of disassembly (Figure 4G). These data show that the observed viral particles in late endosomes were exposed to a low pH environment, resulting in the partial disassembly of the M1 scaffolding layer and extensive conformational changes of the HA glycoprotein, rendering it to a disorganized and fusion-competent state. Importantly, IAVs were frequently observed in close contact with ILVs and the endosomal limiting membrane. These sites showed membrane merger, displaying a typical structure of hemifusion intermediates between viral and endosomal membranes (Figure 4I–L) consistent with hemifusion diaphragms formed *in vitro* between influenza VLPs and liposomes (Chlanda et al., 2016). The observed structures of arrested hemifusion allow for lipid exchange between the viral and endosomal membrane, which is in accord with live-cell fluorescence microscopy studies (Desai et al., 2014). No fused IAV or vRNPs were observed in the cytosol, illustrating that IFITM3 can effectively block the membrane fusion of most incoming viruses. The majority (65%, n = 28) of the contact sites were observed between viral particles and ILVs (Figure 4I and 4J, Figure S10). In contrast, only a smaller fraction (14%, n = 6) was found in contact with the limiting late endosomal membrane (Figure 4K and 4L, Figure S11), suggesting that ILVs can frequently serve as a fusion target for IAV. These data show that IFITM3 does not only block viral entry via fusion with the limiting late endosomal membrane but can also block indirect entry pathways through fusion with ILVs and subsequent back-fusion of ILVs with the limiting late endosomal membrane. Thus IFITM3 can likely impede the endosomal escape of different viruses which are known to hijack the back-fusion pathway (Le Blanc et al., 2005) by blocking membrane

fusion with ILVs. This is in accord with a recent study showing that IFITM3 prevents ILV back-fusion (Perrin et al., 2021).

In summary, *in situ* cryo-ET revealed that IFITM3 expression stabilizes the hemifusion state one hour post IAV infection in both the endosomal limiting membrane and at the membranes of ILVs in the late endosomal lumen. This validates the prediction by continuum modelling that the dwell time is increased (Figure 3H).

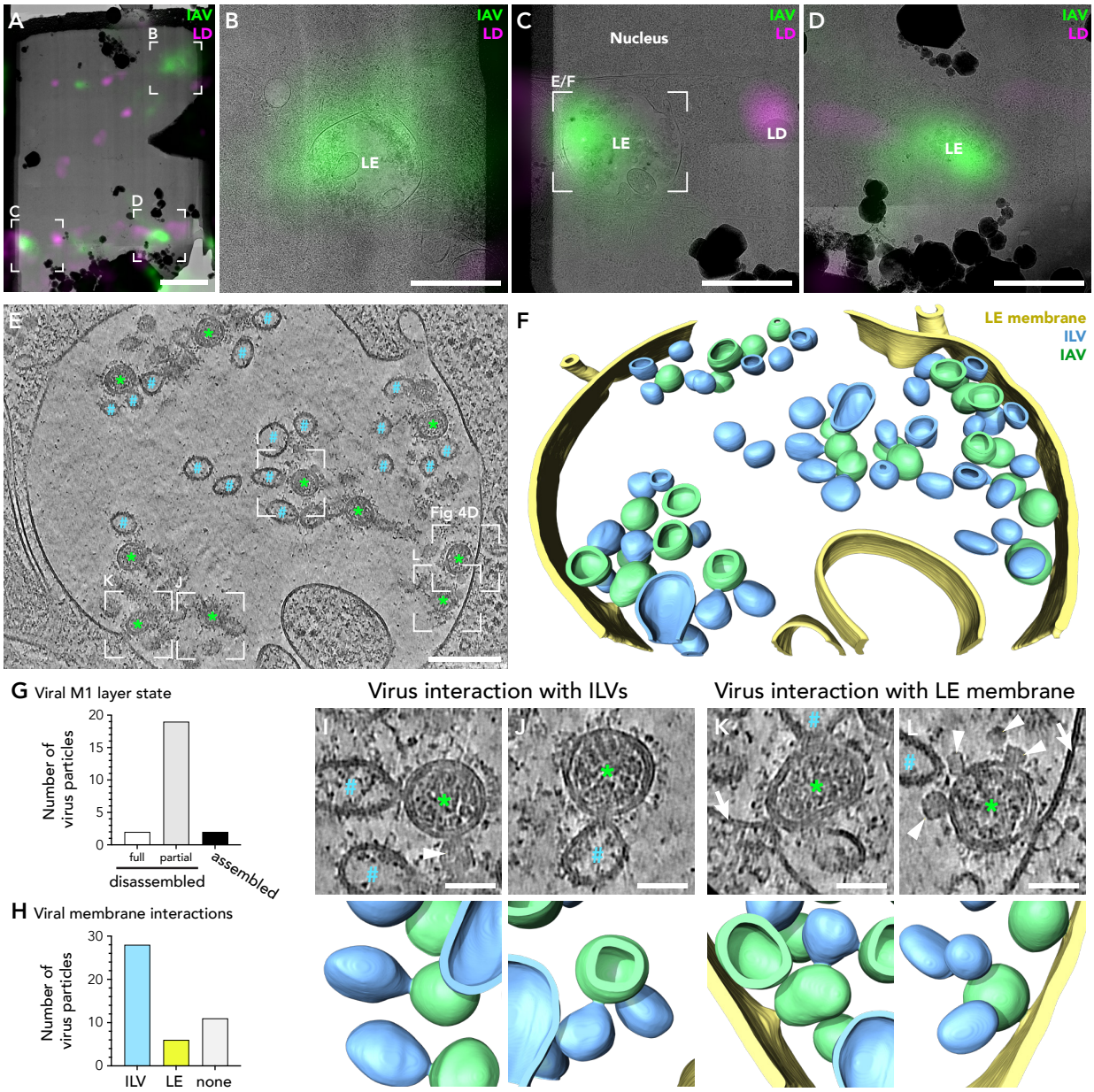

Figure 4. IFITM3 stabilizes hemifusion intermediates during IAV mediated fusion with the late endosomal limiting membrane and ILVs. **(A)** Cryo-lamella of an A549-IFITM3 cell infected with fluorescently labeled influenza

virus A/WSN/1933-nDiO (MOI = 200, 1 hpi). Lipid droplets (LDs) were fluorescently labeled and used as fiducial markers for *in situ* cryo-CLEM. The fluorescent signal of IAV is shown in green. The LD signal is shown in magenta. **(B–D)** Magnified areas of the correlated cryo-lamella shown in (A). Late endosomes (LE) with a typical multivesicular morphology were found positive for fluorescent IAV signal. One correlated LD is shown in (C). **(E)** Tomographic slice (5.34 nm thickness) of a late endosome correlated to the IAV fluorescence signal (C). The late endosomal lumen incorporates ILVs (blue hashes) and IAV particles (green asterisks). To increase the signal-to-noise ratio, reconstructed tomograms were SIRT-like filtered and denoised using cryoCARE. See Video S1 for three-dimensional rendering. **(F)** The three-dimensional volume segmentation of the tomogram is shown in (E). The late endosomal membrane is shown in yellow, IAV particles in green, and ILVs in blue. **(G)** Quantification of the morphology of the scaffolding M1 layer state of IAV particles in late endosomes. M1 was classified as assembled or disassembled (fully/partially). **(H)** Quantification of interactions between IAV particles and cellular membranes. Viral particles were either in contract with intraluminal vesicles (ILV, blue) or the limiting late endosomal membrane (LE, yellow). **(I–L)** Magnified areas of reconstructed tomogram (E) showing two exemplary stabilized hemifusion sites between IAV particles and ILVs (I and J) and between IAV particles and the limiting late endosomal membrane (K and L). Virus particles are indicated with green asterisks and ILVs with blue hashes. The limiting late endosomal membrane is indicated with white arrows (K, L). Crystal-like structures (white arrowheads) were regularly observed in contact with ILV particles (white arrowheads). For each tomogram, the three-dimensional volume segmentation is shown below. See Figure S10 and Figure S11 for a gallery of all sites of stabilized hemifusion. Scale bars: (A) 3 µm, (B–D) 1 µm, (E, F) 200 nm, (I–L) 50 nm.

Stabilized hemifusion diaphragms show symmetric geometry and a high energy barrier for fusion pore formation

The hemifusion sites visualized by *in situ* cryo-ET showed an axial symmetry around the central axis, and their geometry could be quantified from our tomograms. Measurements of the hemifusion sites (n = 17) (Figure 5A–C) revealed a narrow average outer angle of 63° (SD = 12°) and wide inner viral and cytoplasmic angles of 157° (SD = 11°) and 140° (SD = 13°), respectively. As no significant differences were observed between opposing contact angles, the hemifusion sites were either formed by symmetric expansions or converged into a favorable symmetric geometry (Risselada and Grubmüller, 2021). The average hemifusion diaphragm diameter measured from the phospholipid head groups was 16.5 nm (SD = 5.3 nm, n = 17), consistent with stable hemifusion diaphragms observed *in vitro* (Chlanda et al., 2016). The observed hemifusion site geometry allowed us to assess, based on the geometry of the hemifusion diaphragm, the stress in the hemifusion diaphragm and the fusion-pore formation energy as 113 k_BT (SD = 44 k_BT, n = 16) (Figure S11). This energy barrier is higher than the energy barrier estimated by our simulations (40 k_BT with no IFITM3 and 46 k_BT with 0.32% IFITM3, Figure 3F). However, the energy barrier generated by our simulations strongly depends on the lipid composition in the late endosome and the monolayer tilt and bending rigidities, so an exact comparison between theory and experiment is challenging. For

example, the theory predicted that the energy barrier reaches 113 k_BT if we consider 40% cholesterol (instead of 30%) and 0.07% IFITM3 (Figure S4 E) or by considering lipid tilt decay length of 1.5 nm (instead of 1.2 nm used in the simulations, the range reported in the literature is 1 – 2 nm (Terzi and Deserno, 2017)) and 0.26% IFITM3 (Figure S4F). Therefore, based on the cryo-ET results, it is likely that either the cholesterol fraction in the late endosome or the tilt decay length in our model is underestimated.

In summary, our *in situ* cryo-ET data support the continuum membrane modeling data. It shows IFITM3-induced stabilized hemifusion sites and an increased energy barrier for the fusion-pore formation and subsequent increased dwell time for membrane fusion, as predicted by our theoretical model (Figure 4F and 4H).

Post-fusion HA is confined in stabilized hemifusion diaphragms

Intriguingly, regular cylindrical densities orthogonal to the hemifusion diaphragms were frequently observed (Figure 5D and 5E, red arrow) at both ILV membranes (Figure S10, red arrows) and late endosomal membranes (Figure S11, red arrows). As these densities likely represent HA glycoproteins that underwent conformational changes, we utilized subtomogram averaging to investigate the conformational status. Subvolume extraction and iterative averaging of potential HA glycoproteins localized at hemifusion diaphragms (n = 30) revealed a rod-shaped structure featuring a stalk and head (Figure 5F and 5G, Figure S12, Video S5) with a dimension of 13.6 × 5.1 × 5.0 nm, overall consistent with the HA post-fusion conformation, which was also determined recently by single-particle cryo-EM (Benton et al., 2020). The crystal structure of the post-fusion HA2 (Chen et al., 1999) was fitted to the electron density of the subtomogram average (Figure 5E) with high accuracy (97.1% atoms inside the isosurface). Hence, the observed density at the hemifusion diaphragm likely represents the viral HA glycoprotein in its post-fusion state. No densities corresponding to HA1 subunits were evident, presumably due to HA1 dissociation at reducing condition of endosomes (Hastings and Cresswell, 2011). In addition to the HA2 density, the average revealed both the endosomal and the viral membranes (Figure S12A, green dotted lines), confirming the high symmetric geometry of the hemifusion sites. On two occasions, the outer membrane dome protein (OMDP), a protein complex previously characterized by us (Klein et al., 2021b), was observed on the cytosolic site of the hemifusion site (Figure 5D and 5E, cyan arrows). However, since our data show that IFITM3 blocks membrane fusion also in the absence of OMDPs, it is unlikely that OMDPs play an important role in the antiviral function of IFITM3.

Overall, our findings show that IFITM3 does not exclude the viral fusion machinery from the fusion sites. Furthermore, IFITM3 does not interfere with the conformational transitions of the viral fusion protein. Hence the HA machinery could provide energy that under non-inhibitory circumstances would lead to membrane fusion and pore formation. This argues for the role of the IFITM3-lipid sorting activity in stabilizing the hemifusion state and shows that IFITM3 can inhibit a broad variety of viral fusion proteins.

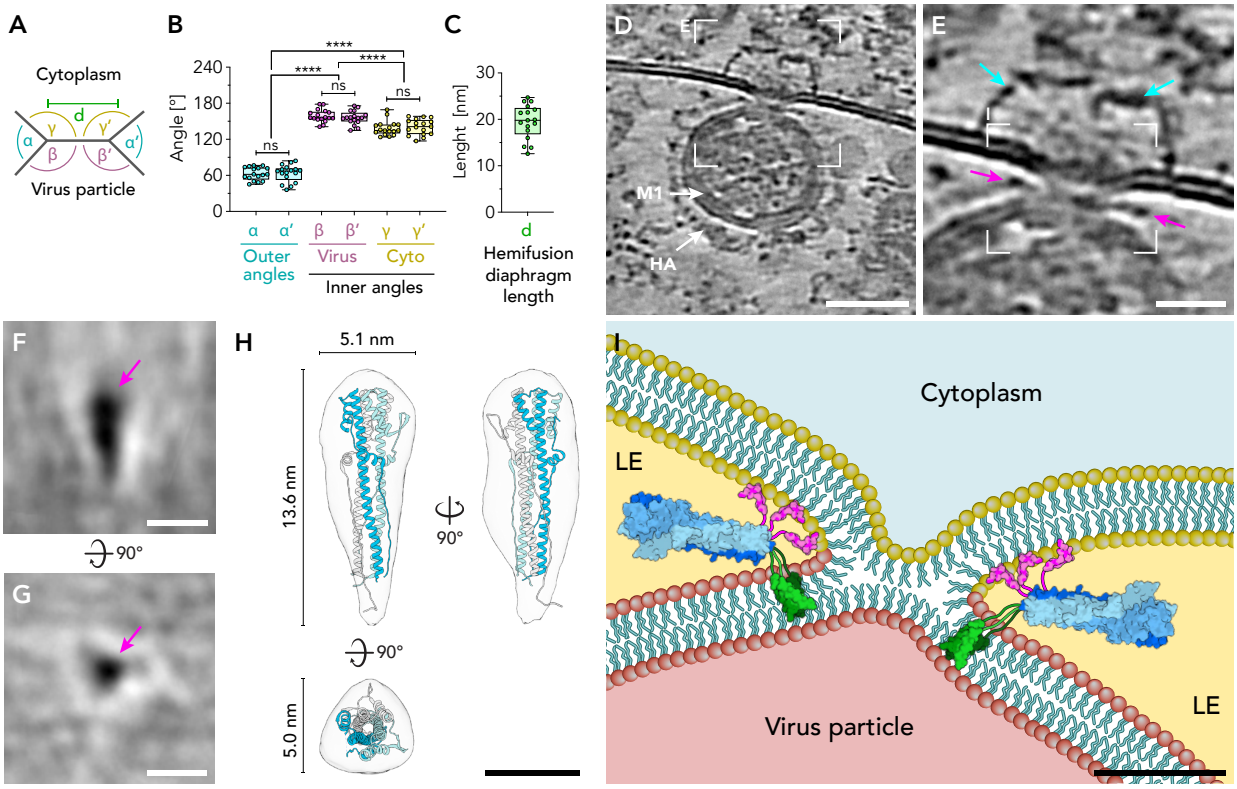

Figure 5. Post-fusion HA glycoproteins are localized at the hemifusion diaphragm. **(A–C)** The geometry of hemifusion diaphragms was analyzed by measurements of angles (B) and diaphragm size (C) for individual hemifusion sites (n = 17). The following angles are defined as indicated in the schematic (A): Outer angles (α and α'), inner angles facing the viral lumen (β and β'), and inner angles facing the cytoplasm (γ and γ'). Paired t-test was performed to analyze the significance of the difference between pairs of angles and between groups of angles. Data is shown as Box and Whiskers plots indicating the median (center of box), 25% and 75% quartiles (bounds of box), minimum and maximum values (bars), and all data points. **(D)** Magnified area of reconstructed tomogram (Figure 4E) showing a stabilized hemifusion site between IAV particle and late endosomal membrane. The image is rotated 90° compared to Figure 4E. The virus particle shows a low pH morphology with disorganized HA and partially disassembled M1 layer. **(E)** Magnified area of the hemifusion diaphragm between the late endosomal membrane and virus particle (D). Electron dense structures are localized orthogonal to the hemifusion diaphragm (magenta arrows), representing post-fusion HA glycoproteins at the diaphragm region. Close to the hemifusion site, two OMDPs were observed (cyan arrow). **(F–H)** Subtomogram average of post-fusion HA localized at the hemifusion diaphragm. 30 subvolumes were extracted and averaged. Central slices of the subtomogram average for side-view (F) and top-view

(G) are shown. The electron-dense post-fusion HA is localized in the center (magenta arrow). The post-fusion HA2 structure (PDB: 1QU1, Chen et al., 1999) was fitted to the three-dimensional isosurface of the subtomogram average (H). See Figure S13 for all iterative steps of the subtomogram average analysis. **(I)** A model of the stabilized hemifusion diaphragm is shown in panel E (white square). Late endosomal phospholipids are shown in yellow and viral phospholipids in red. Lumina of the virus particle, cytoplasm, and late endosome (LE) are indicated. The trimeric post-fusion HA glycoprotein model without fusion peptide (PDB: 1QU1, Chen et al., 1999) is shown in blue, with each monomer shown in a different shade of blue, fusion peptides are shown in magenta (PDB: 1QU1, Chen et al., 1999). The transmembrane domain of HA is shown in green (PDB: 6HJR, Benton et al., 2018). Positions of transmembrane domain and fusion-peptides are assumed, as they are not resolved in the tomographic data. Statistical significance: * for $p < 0.05$, ** for $p < 0.01$, *** for $p < 0.001$ **** for $p < 0.0001$. Scale bars: (D) 50 nm, (E) 20 nm, (F and G) 10 nm, (H) 5 nm, (I) 10 nm.

CONCLUSIONS

IFITM3 has evolved as a broad and unspecific host countermeasure against a wide range of viruses that enter the cell via the late endosomal pathway, like IAV, West Nile virus, Chikungunya virus, respiratory syncytial virus (Zani and Yount, 2018), tick-borne encephalitis virus (Chmielewska et al., 2022) as well as Marburg and Ebola filoviruses (Huang et al., 2011). Therefore, it must function through general principles of viral-host membrane fusion inhibition. However, despite its substantial medical importance, the underlying principles were not understood. In this study, we showed that the number of ILVs in the late endosomal lumen is not modulated by IFITM3, which contradicts the 'fusion decoy' model (Desai et al., 2014). As cholesterol is well known to modulate membrane properties by increasing membrane rigidity and spontaneous negative curvature (Yang et al., 2016), we analyzed the interaction between IFITM3 and cholesterol and found specific interactions between cholesterol and IFITM3. Atomistic MD simulations revealed that cholesterol specifically interacts with the palmitoylated Cys72, which was recently identified as essential for the antiviral properties of IFITM3 (Garst et al., 2021). Furthermore, atomistic MD simulations in lipidic systems mimicking an endosomal membrane composition and binary POPC–cholesterol mixtures show that IFITM3, despite the interaction of cholesterol with palmitoylated Cys72, overall repels cholesterol from its vicinity. Since IFITM3 is excluded from the hemifusion diaphragm due to its transmembrane domain and the structure of the hemifusion diaphragm rim, our MD simulations data indicates that IFITM3 can locally modulate the bilayer lipid composition and thereby withdraw fusion pore driving lipids from the hemifusion diaphragm. Continuum membrane modeling suggests that IFITM3-induced lipid sorting increases the energy barrier of fusion pore formation by up to 17 $k_BT/(mol_{IFITM3}\ \%)$. This outpowers the viral fusion machinery's energy and thus stabilizes the hemifusion state, leading up to a 14-fold

increased dwell time for a modest IFITM3 concentration of 0.16 mol%. This increased dwell time allows for the degradation of virus particles in lysosomes and effectively blocks viral entry. To validate the MD simulations and membrane modeling data, we directly visualized stabilized hemifusion during viral-induced membrane fusion in late endosomes of IFITM3 overexpressing A549 cells using correlative *in situ* cryo-ET, which revealed IAV arrested at the hemifusion state, hence confirming the previously proposed hypothesis of 'hemifusion stabilization' (Desai et al., 2014). Furthermore, subtomogram averaging revealed post-fusion HA localized close to the hemifusion sites, providing direct evidence that IFITM3 does not affect the fusogenic activity of the viral fusion protein. Since the backfolding of the extended HA intermediate to the coiled-coil post-fusion state is not inhibited, the energy released during this irreversible process was not sufficient to overcome the energy barrier for fusion pore formation, supporting the IFITM3-induced lipid-sorting as the principal inhibitory mechanism of IFITM3.

ACKNOWLEDGMENTS

We want to thank Frank Orth for the cover art. We acknowledge access to the infrastructure and support provided by the Infectious Diseases Imaging Platform (IDIP) at the Center for Integrative Infectious Disease Research Heidelberg (Germany), the Cryo-EM Network at the Heidelberg University (HD-cryoNet) (Germany), the Electron Microscopy Core Facility at EMBL Heidelberg (Germany), the computational resources at CSC-IT Centre for Science Ltd. (Espoo, Finland) and IT support at BioQuant Heidelberg (Germany). We want to thank Dr. Marco Binder for access to the cDNA library and plasmids for lentiviral production, Prof. Dr. Ervin Fodor for providing plasmids for A/WSN/1933 reverse genetics system, and Prof. Dr. Andrew Mehle for providing plasmids for the fluorescently tagged PA. We are grateful to Hwayoung Lee, Prof. Wonpil Im, and Prof. Howard Hang for providing us with the Cys72 palmitoylated IFITM3 initial structure for performing atomistic MD simulations. This work was supported by a research grant from the Chica and Heinz Schaller Foundation (Schaller Research Group Leader Program) to P.C., N.R., R.B, C.L. and A.K. In addition, this work was funded by the Deutsche Forschungsgemeinschaft (DFG, German Research Foundation) Sonderforschungsbereich (SFB, Collaborative Research Centre) 1129 to Y.S., B.B., U.S.S., P.C. and S.K; SFB TRR83 to F.L. and W.N.; DFG Ni 423/10-1 to D.B. and W.N.; DFG-FNR EMSIVILIN to M.W.-M.; G.G. acknowledges support by the Minerva Stiftung. The authors gratefully acknowledge the data storage service SDS@hd supported by the Ministry of

Science, Research, and the Arts Baden-Württemberg (MWK) and the DFG through grant INST 35/1314-1 FUGG and INST 35/1503-1 FUGG.

AUTHOR CONTRIBUTIONS

Steffen Klein: Conceptualization; Investigation and formal analysis (creating stable cell line and reporter virus, confocal microscopy, BlaM assay, immunoblotting, infection assay, ET, cryo-CLEM, cryo-ET, STA); Visualization; Writing - Original Draft. **Gonen Golani:** Investigation and formal analysis (membrane modeling and theory, cholesterol affinity and repulsion model, energy barrier calculation from cryo-ET data); Writing - Original Draft. **Fabio Lolicato**: Investigation and formal analysis (MD simulations design, computational resources, data curation, methodology); Writing - Original Draft. **Daniel Beyer:** Investigation and formal analysis (systems preparation and equilibration for MD simulations). **Alexia Herrmann:** Investigation and formal analysis (cholesterol labeling and IP). **Moritz Wachsmuth-Melm:** Formal analysis (cryo-ET). **Nina Reddmann:** Investigation (creation of stable cell line and reporter virus). **Romy Brecht:** Investigation (creation of stable cell line, BlaM assay). **Carmen Lahr:** Investigation (creation of reporter virus, infection assay). **Mehdi Hosseinzadeh:** Formal analysis (ET). **Androniki Kolovou:** Investigation (HPF/FS sample preparation). **Martin Schorb:** Investigation (ET data acquisition). **Yannick Schwab:** Writing - Review & Editing. **Britta Brügger:** Writing - Review & Editing. **Walter Nickel:** Writing - Review & Editing. **Ulrich Schwarz:** Writing - Review & Editing. **Petr Chlanda:** Conceptualization; Funding acquisition; Supervision; Writing - Original Draft; Writing - Review & Editing.

DECLARATION OF INTERESTS

The authors declare no competing interests.

METHODS

Resource availability

Lead contact

Further information and requests for resources and reagents should be directed to and will be fulfilled by the lead contact, Petr Chlanda (chlanda@bioquant.uni-heidelberg.de).

Materials availability

All materials are available on request.

Data and code availability

MD simulations parameters and structures files are publicly available at Zenedo: https://doi.org/10.5281/zenodo.6599836. The MATLAB code for all modeling simulations are publicly available on GitHub at the following address: https://github.com/GonenGolani/Fusion_Solver. All reconstructed *in-situ* cryo-electron tomograms are available at the Electron Microscopy Data Bank (EMDB) (Lawson et al., 2016) with the following accession codes: EMD-15130 (for Figure 4E), EMD-15131 (for Figure S7), EMD-15132 (for Figure S8), EMD-15133 (for Figure S9). All reconstructed tomograms of HPF/FS samples are available at EMDB with the following accession codes: EMD-15705 (for Figure 1R), EMD-15707 (for Figure 1T), EMD-15708 (for Figure 1V). All fluorescence microscopy (Figures 1B, 1D, 1F, 1I, 1L, S1D and S1H) and immunoblot data (Figures 1A and 2A) are available at the BioStudies database (Sarkans et al., 2018) with the accession code S-BIAD539.

Experimental model and subject details

Human embryonic kidney 293 cells expressing SV40 large T antigen (HEK293T)

HEK293T cells were obtained from the American Type Culture Collection (ATCC). Cells were cultured at 37 °C in 5% CO_2 in Dulbecco's modified Eagle medium (DMEM) supplemented with GlutaMAX™-I, 10% fetal bovine serum (FBS), and 1% penicillin/streptomycin (P/S).

HEK293T-Master Cell Bank cells (HEK293T-MCB)

HEK293T-MCB cells were kindly provided by Dr. Marco Binder (DKFZ, Heidelberg, Germany). Cells were cultured at 37 °C in 5% CO_2 in DMEM supplemented with GlutaMAX™-I, 10% FBS, and 1% P/S.

Madin-Darby canine kidney cells (MDCK)

MDCK cells were kindly provided by Prof. João Amorim (Instituto Gulbenkian de Ciência, Portugal). Cells were cultured at 37 °C in 5% CO_2 in DMEM-F12 supplemented with 10% FBS and 1% P/S.

A549 cells

A549 is a cell line derived from carcinomatous lung tissue from a Caucasian male at age 58 (Giard et al., 1973) and is regularly used as a model cell line for IAV infection studies. Cells were obtained from ATCC and cultured at 37 °C in 5% CO_2 in DMEM-F12 supplemented with 10% FBS and 1% P/S.

A549 cells expressing IFITM3 (A549-IFITM3)

To study the antiviral effect of IFITM3, we established an A549 cell line stably overexpressing IFITM3 using lentiviral transduction, as described in the following section.

Cloning: The IFITM3 gene sequence, including a stop codon, was transferred from a cDNA entry vector (pENTR221-clone3728-IFITM3) to the destination vector pWPI-IRES-Puro. 150 ng of entry and destination vector were added with 1 µl Gateway™ LR Clonase Enzyme Mix (ThermoFisher Scientific, Invitrogen) in a total volume of 5 µl TE buffer (10 mM Tris, 0.1 mM EDTA, pH 8). The reaction was run for 2 h at 25 °C on a thermocycler.

Transformation: 50 µl *E. coli* Stellar™ competent cells (Takara) were combined with 5 µl reaction mix from the cloning step and incubated for 30 min on ice and subsequently heat shocked for 45 sec at 42 °C on a heating block. 450 µl S.O.C. medium (ThermoFisher Scientific, Invitrogen) was added, cells were transferred to a 14 ml round bottom tube and incubated for 1 h at 37 °C on a shaker with 180 rpm. Cells were plated on 1.5% LB agar plates with 50 µg/ml ampicillin and incubated overnight at 37 °C. Individual colonies were picked, added to 50 ml LB media containing 50 µg/ml ampicillin, and incubated for 16 h at 37 °C on a shaker with 180 rpm. Plasmids were purified using the QIAprep Spin Miniprep Kit (QIAGEN), and individual clones were sequenced at Microsynth using the IRES-rev primer (TATAGACAAACGCACACCG). The correct insert was validated, and a second 200 ml overnight

culture was purified using the Plasmid Maxi Kit (QIAGEN). The new plasmid is named pWPI-IFITM3.

Lentiviral production: All work with infectious lentiviruses was performed under biosafety level 2 (BSL-2) laboratory conditions. Lentivirus was produced using a second-generation packaging system utilizing the envelope plasmid pCMV-VSV-G, the packaging plasmid psPAX2, and the previously cloned transfer plasmid pWPI-IFITM3. For enhanced protein expression, we further used the pAdVantage™ plasmid (Promega). HEK293T-MCB cells were seeded in a 6-well plate with 4×10^5 cells per well in a 2.5 ml cell culture medium (DMEM-GlutaMAX™-I, 10% FBS, 1% P/S) and incubated overnight at 37 °C with 5% CO_2. The transfection mix was prepared as follows for one well: 0.375 µg pCMV-VSV-G plasmid, 0.75 µg psPAX2 plasmid, 1.25 µg pWPI-IFITM3 plasmid, 0.125 µg pAdVantage™ plasmid were added in 250 µl Opti-MEM medium (ThermoFisher Scientific, Gibco). 7.5 µl transfection reagent TransIT-2020 (Mirus Bio) was added and incubated for 30 min at RT. The transfection mix was added to one well of the 6-well plate. 6 h post-transfection, the cell culture medium was replaced with 1.5 ml fresh medium. 48 h post-transfection, lentivirus containing supernatant was harvested and filtered through a 0.45 µm CME filter (Roth). A Lenti-X™ GoStix (Takara) antigen test was used to verify successful lentivirus production.

Transduction: A549 cells were seeded in a 12-well plate with 2×10^4 cells per well in 1 ml cell culture medium (DMEM-F12, 10% FBS, 1% P/S) and incubated overnight at 37 °C with 5% CO_2. 350 µl filtered lentivirus supernatant was supplemented with polybrene infection reagent (Merck, Sigma-Aldrich) in a final concentration of 5 µg/ml. The cell culture medium of A549 cells was removed, and 350 µl lentivirus supernatant was added to the cells. 2 days post-transduction, the antibiotic selection was started with 0.8 µg/ml puromycin. After 2 days of selection, the puromycin concentration was increased to 1.2 µg/ml. The selection was continued for 2 more days until all non-transduced control cells detached from the dish. Selected cells were trypsinized and transferred to a 10 cm cell culture dish and were further grown in a selection medium with 1.5 µg/ml puromycin. Individual cell colonies could be observed after 2 more days. Individual colonies were separated using cloning cylinders (Sigma-Aldrich) and further expanded to establish the monoclonal cell line A549-IFITM3.

Influenza A virus (strain A/WSN/1933)

Reverse genetics: All work with infectious IAV was performed under BSL-2 laboratory conditions. The IAV strain A/WSN/1933 (H1N1) was rescued from a reverse genetics system established by Hoffmann et al., 2000. 4×10^6 HEK293T cells were seeded in a 10 cm cell

culture dish and grown overnight in 10 ml complete growth media (DMEM-GlutaMAX™-I, 10% FBS, 1% P/S). The transfection mix was prepared as follows: 2.5 µg of each of the 8 plasmids of the reverse genetics system (pHW2000-PB1-WSN, pHW2000-PB2-WSN, pHW2000-PA-WSN, pHW2000-NP-WSN, pHW2000-NA-WSN, pHW2000-M-WSN, pHW2000-NS-WSN, pHW2000-HA-WSN) were added to a total volume of 2 ml Opti-MEM medium. 60 µl transfection reagent TransIT-293 (Mirus Bio) was added and incubated for 30 min at RT and added to the 10 cm dish with HEK293T cells. After 24 h, the medium was exchanged with FBS-free infection medium (DMEM-GlutaMAX™-I, 1% P/S, 0.3% BSA, 2 µg/ml TPCK-trypsin), and 4 × 10^6 MDCK cells were seeded in the same cell culture dish to be co-cultured with the transfected HEK293T cells. After 24 h, virus-containing supernatant (P0) was harvested and centrifuged for 10 min with 1,000 × g to remove cell debris. The supernatant was aliquoted, shock frozen in LN_2, and stored at -80 °C until further use.

Virus propagation and purification: 6 × 10^6 MDCK cells were seeded in 30 ml complete growth media (DMEM-GlutaMAX™-I, 10% FBS, 1% P/S) in T175 cell culture flasks and grown overnight. The virus-containing supernatant (P0), recovered from the reverse genetics system, was diluted 1:10 in FBS-free infection media (DMEM-GlutaMAX™-I, 1% P/S, 0.3% BSA, 2 µg/ml TPCK-trypsin). MDCK cells were washed 3 times with PBS. 10 ml of the diluted virus supernatant was added to the cells and incubated for 1 h at 37 °C with 5% CO_2. Cells were washed 1 time with PBS, and 40 ml FBS-free infection medium was added. Cells were grown for 3 days until a cytopathic effect was observed. The virus-containing supernatant (P1) was centrifuged 2 times for 15 min at 2,200 × g to remove cell debris. Cleared supernatant was subsequently sucrose purified: 33 ml of virus-containing supernatant was overlaid on 5 ml of 30% sucrose in HEN buffer (10 mM HEPES, 1 mM EDTA, 100 mM NaCl, pH 7.4) in a thin-walled centrifugation tube and centrifuged for 90 min at 83,018 × g, 4 °C using the swing-out rotor SW32 on an Optima L-90K (Beckman Coulter) ultracentrifuge. The supernatant was discarded, and the pellet was resuspended in 1 ml HEN buffer. The sample was centrifuged again for 30 min at 15,728 × g, 4 °C using the fixed-angle rotor TLA-120.2 on an Optima TLX (Beckman Coulter) ultracentrifuge. The supernatant was discarded, and the pellet was dissolved in 200 µl HEN buffer. The purified virus was aliquoted, shock frozen in LN2, and stored at -80 °C until further use.

Plaque assay: 1 × 10^6 MDCK cells per well were seeded in a 6-well plate in 2 ml complete growth medium (DMEM-F12, 10% FBS, 1% P/S) and grown overnight. Dilution series of purified virus stock was prepared in an FBS-free infection medium (DMEM-GlutaMAX™-I, 1% P/S, 0.3% BSA, 2 µg/ml TPCK-trypsin) from 10^{-3} to 10^{-9}. Cells were washed 3 times with PBS,

and 800 µl of each virus dilution was added per well. Cells were incubated for 1 h at 37 °C and 5% CO_2, virus dilution was removed, cells were washed 2 times with infection medium and overlayed with 3 ml plaque medium containing Avicel (DMEM-GlutaMAX™-I, 0.5% P/S, 0.15% BSA, 1 µg/ml TPCK-trypsin, 1.2 % Avicel RC-581) per well. After 2 days, the plaque medium was aspirated, and cells were washed 2 times with PBS and fixed with 1% glutaraldehyde (GA) in PBS for 30 min at RT. Cells were washed with PBS and stained with 1% crystal violet solution (Sigma-Aldrich) for 10 min at RT. Cells were thoroughly washed with water, and plaques were counted. For each dilution, virus titer, T_{virus}, was determined by $T_{virus} = \frac{n_{plaque}}{d*V}$, with the number of plaques, n_{plaque}, the dilution factor, d, and the volume of virus dilution, V. The average titer of all wells containing plaques was determined and used as final virus titer.

Fluorescently labeled influenza A virus (A/WSN/1933-nDiO)

For *in situ* cryo-CLEM, we fluorescently labeled A/WSN/1933 IAV using the fluorescent and lipophilic membrane dye neuro-DiO (nDiO). The virus was recovered from a reverse genetics system and purified as described above. 5 µl of ready to use nDiO solution 'Cellbrite™ Green' (Biotium) was added to 200 µl purified virus and incubated for 1 h on a rotation wheel at RT. The virus was subsequently purified again by sucrose purification: 200 µl purified and fluorescently labeled virus was overlaid on 500 µl of 10% sucrose in HEN buffer in a thick-walled centrifugation tube and centrifuged for 90 min at 107,000 × g, 4 °C using the swing-out rotor TLS-55 on an Optima Max (Beckman Coulter) ultracentrifuge. The supernatant was discarded, and the pellet was resuspended in 1 ml HEN buffer. The sample was centrifuged again for 30 min at 15.728 × g, 4 °C using the fixed-angle rotor TLA-120.2 on an Optima TLX (Beckman Coulter) ultracentrifuge. The supernatant was discarded, and the pellet was dissolved in 200 µl HEN buffer. The fluorescently labeled virus was aliquoted, shock frozen in LN_2, and stored at -80 °C until further use. Viral titer was determined again using the plaque assay as described above.

Fluorescent influenza a reporter virus (A/WSN/1933-PA-mScarlet)

For the infection assay, we established a reporter virus A/WSN/1933 expressing a fluorescently tagged polymerase acidic protein (PA) based on Tran et al., 2013. For increased integration stability of the fluorescent tag in the viral genome, we performed codon optimization of the gene sequence coding for the fluorescent protein mScarlet by substitution

of CpG and TpA sites, which are known to be recognized by the Zinc finger antiviral protein restriction factor (Odon et al., 2019).

mScarlet codon optimization: The gene sequence coding for mScarlet (Bindels et al., 2016) was codon-optimized for mammalian gene expression using the GenSmart™ codon optimization algorithm (version 1.0, GenScripts). Subsequently, all CpG and TpA sites in the codon-optimized sequence were manually exchanged without modifying the aminoacidic sequence. This optimized sequence was synthesized and inserted in a pcDNA3.4 plasmid by the GeneArt gene synthesis service (ThermoFisher Scientific). The newly synthesized plasmid is named pcDNA3.4-mScarlet-codon-optimized.

Cloning: Using In-Fusion cloning (Takara), we exchanged the mScarlet of the reverse genetics' plasmid pHW2000-PA-mScarlet (kindly provided by Prof. Dr. Andrew Mehle) with the codon-optimized mScarlet, generated as described above. Overhang PCR was prepared as follows: 1 ng pcDNA3.4-mScarlet-codon-optimized plasmid, 0.2 µM forward overhang primer (CCCACGCCCTGCGCGCGGCAGCAATGGTGTCCAAGGGTGAAGC), 0.2 µM reverse overhang primer (AAGCAGTTTTCTAGATCACTTGTACAGCTCATCCATTCCAC), 12.5 µl CloneAmp™ HiFi PCR Premix (Takara) and 1 µl DMSO were mixed in a total volume of 25 µl H_2O. PCR reaction was run for 35 cycles with denaturation at 98 °C for 10 sec, annealing at 64 °C for 15 sec, and elongation at 72 °C for 10 sec. 8 µl Cloning Enhancer (Takara) was added to 20 µl of the PCR product and incubated for 15 min at 37 °C on a thermocycler, followed by an inactivation step at 80 °C for 15 min. The pHW2000-PA-mScarlet plasmid was linearized by restriction digestion: 1 µg pHW2000-PA-mScarlet plasmid, 1 u XbaI (New England Biolabs), 1.33 u BssHII (New England Biolabs) were added in a total of 50 µl 1× CutSmart buffer (New England Biolabs). The reaction was run for 15 min at 37 °C on a thermocycler, followed by an inactivation step at 65 °C for 20 min. Restriction digestion products were separated on a 0.7% agarose gel, and linearized plasmid was purified from the gel using the NucleoSpin Gel and PCR Clean-up kit (Macherey-Nagel). In-Fusion reaction was prepared as follows: 25 ng PCR fragment with overhang, 50 ng linearized and purified vector, 1 µl 5× In-Fusion Enzyme Mix (Takara) were mixed in a total of 5 µl H_2O. The reaction was run for 15 min at 50 °C on a thermocycler.

Transformation: 50 µl *E. coli* Stellar™ competent cells (Takara) were combined with 5 µl In-Fusion reaction product and incubated for 30 min on ice and subsequently heat shocked for 45 sec at 42 °C on a heating block. 450 µl S.O.C. medium (ThermoFisher Scientific, Invitrogen) was added, cells were transferred to a 14 ml round bottom tube and incubated for 1 h at 37 °C on a shaker with 180 rpm. Cells were plated on 1.5% LB agar plates with 50

μg/ml ampicillin and incubated overnight at 37 °C. Individual colonies were picked, added to 50 ml LB media containing 50 μg/ml ampicillin, and incubated for 16 h at 37 °C on a shaker with 180 rpm. Plasmids were purified using the QIAprep Spin Miniprep Kit (QIAGEN), and individual clones were sequenced at Microsynth using a forward primer (GGCAAACAACAGATGGCTGGCAAC) and reverse primer (GTATGCATCTCCACAACTAGAAGG). The correct sequence was validated, and a second 200 ml overnight culture was purified using the Plasmid Maxi Kit (QIAGEN). The new plasmid is named pHW2000-PA-WSN-mScarlet-codon-optimized.

Reverse genetics: A fluorescent reporter virus was recovered and purified as described above for the A/WSN/1933 virus using the reverse genetics system established by Hoffmann et al., 2000, but here the plasmid pHW2000-PA-WSN was exchanged with pHW2000-PA-WSN-mScarlet-codon-optimized.

Methods details

Immunoblot analysis

The expression levels of IFITM3 in A549 cells, with and without IFNβ treatment, and of the established stable cell line A549-IFITM3 (as described above) were analyzed by immunoblot analysis as described below.

Protein extraction: 1 × 10^6 A549 or A549-IFITM3 cells were seeded in 10 cm cell culture dishes in complete growth medium (DMEM-F12, 10% FBS, 1% P/S). A549 cells were treated with different concentrations of IFNβ (0, 100, 500, 1,000, 2,000 units/ml). After 48 h, cells were washed 2 times with ice-cold PBS and lysed with 650 μl RIPA buffer (50 mM Tris-HCL, 150 mM NaCl, 1% v/v Triton X-100, 0.5% v/v sodium deoxycholate, 0.1% v/v SDS, 1× protease inhibitor cocktail (ThermoFisher Scientific, Roche) in H_2O) on ice for 20 min. The cell lysate was centrifuged with 12,000 × g for 20 min at 4 °C to remove cell debris. The protein concentration of the supernatant was quantified using the Pierce™ BCA Protein Assay Kit (ThermoFisher Scientific).

Gel electrophoresis: All samples were diluted in RIPA buffer to a final protein concentration of 0.7 μg/μl. 66.7 μl 4× Laemmli buffer (Bio-Rad), supplemented with 0.2 M dithiothreitol, was added to 200 μl of diluted sample and incubated for 8 min at 90 °C on a heating block. 40 μl of each sample was loaded to a 4 – 15% precast polyacrylamide gel (Bio-Rad). As a size marker, 10 μl of a broad range color pre-stained protein standard (New England BioLabs) was added to the outer lanes. Samples were separated by gel electrophoresis in 1× TGS running

buffer (Bio-Rad) for 60 min with 120 V using a Mini-PROTEAN electrophoresis chamber (Bio-Rad).

Western-Blotting: Separated proteins were transferred from the polyacrylamide gel to a 0.2 µm PVDF membrane (Bio-Rad) for 7 min with a constant 2.5 A using a Trans-Blot Turbo transfer system (Bio-Rad).

Immunolabeling: PVDF membrane was cut at 26 kDa to analyze the expression of IFITM3 and actin on the same membrane. Membranes were washed 3 times for 5 min in TBS supplemented with 0.1% v/v Tween-20 (TBS-T) and subsequently blocked in 5% BSA in TBS-T for 1 h at RT on a rocker. The lower part of the membrane (0 – 26 kDa) was incubated in primary antibody against IFITM3 (Proteintech) with a dilution of 1:2,000 in TBS-T for 1 h at RT on a rocker. The upper part of the membrane (26 – 250 kDa) was incubated in primary antibody against actin (Sigma-Aldrich) with a dilution of 1:4,000 in TB\parencite{Manuscript.docx} S-T for 1 h at RT on a rocker. Membranes were washed 3 times for 5 min in TBS-T and incubated with the secondary antibodies: anti-rabbit-HRP (Santa-Cruz) with a dilution of 1:1,000 in TBS-T for the lower part of the membrane (0 – 26 kDa), immunolabelled against IFITM3 or anti-mouse-HRP (Santa-Cruz) with a dilution of 1:1,000 in TBS-T for the upper part of the membrane (26 – 250 kDa), immunolabelled against actin, respectively. Membranes were washed 3 times for 5 min with TBS and were subsequently incubated with Clarity Western ECL substrate working solution (Bio-Rad) for 5 min. Chemiluminescent signal was acquired using the Azure 400 imaging system (Azure Biosystems).

Quantification of protein expression: Individual bands of IFITM3 and actin of each sample were quantified using the Gel Analyzer plugin of FIJI (Schindelin et al., 2012). IFITM3 signal was normalized to the corresponding actin, and relative IFITM3 expression levels were calculated.

Confocal fluorescent light microscopy

Confocal fluorescent light microscopy analysis was performed to study the impact of IFNβ treatment or IFITM3 overexpression on the number and volume of IFITM3 positive organelles in A549 cells.

Immunofluorescence: 5×10^4 A549 or A549-IFITM3 cells were seeded on 12 mm microscopy coverslips NO. 1 (Marienfeld) in a 6-well plate in complete growth medium (DMEM-F12, 10% FBS, 1% P/S). The next day, A549 cells were treated with 1×10^3 units/ml IFNβ (Immuno

Tools). After 24 h IFNβ treatment, cells were fixed with 4% PFA in PBS for 15 min and washed 3 times with PBS. PFA was quenched by incubating the cells with 20 mM glycine in PBS for 10 min, followed by 3 washing steps with PBS for 5 min each. Cells were permeabilized by incubation with 0.2% Triton X-100 in PBS for 5 min, followed by 3 washing steps with PBS for 5 min each. Cells were incubated for 1 h with blocking buffer (3% BSA in PBS supplemented with 0.1% Tween-20 (PBS-T)). After 3 short washing steps with PBS-T, cells were incubated for 1 h with primary antibody against IFITM3 (Proteintech) using an antibody dilution of 1:200 in dilution buffer (1% BSA in PBS-T) at RT on a rocker. After 3 washing steps with PBS-T for 5 min each, cells were incubated with the secondary antibody 'goat anti-Rabbit Alexa Fluor™ 633' (ThermoFisher Scientific, Invitrogen) in a dilution of 1:2,000 in dilution buffer for 1 h at RT on a rocker. After 3 washing steps with PBS-T for 5 min each, nuclei were fluorescently labeled by incubation with 1 µg/µl Hoechst 33342 (Sigma-Aldrich) in PBS for 5 min. Cells were washed 3 times with PBS for 5 min each, followed by a short washing step with deionized water. Coverslips were mounted on microscopy slides using 7 µl ProLong Glass Antifade mounting medium (ThermoFisher Scientific, Invitrogen). The mounting medium was cured for 24 h at RT.

Confocal microscopy: Confocal microscopy data was acquired using the SP8 TCS laser scanning confocal microscope (Leica) equipped with a 63×/1.4 HC PL APO CS2 oil immersion objective using a UV laser with an excitation wavelength of 405 nm (for Hoechst 33342) and a helium-neon laser with an excitation wavelength of 633 nm (for Alexa Fluor™ 633) in sequential acquisition mode with 4× line accumulation. A pixel size of 60.13 nm was used, and Z-stacks were acquired using a Z-spacing of 200 nm.

Deconvolution: Image stacks were deconvolved with AutoQuant X3 (Media Cybernetics) using a theoretical and adaptive point spread function (PSF) for 10 iterations with the following parameters: lens immersion refractive index 1.515; sample embedding refractive index 1.52; sample distance from coverslip of 0 nm; emission wavelength of 461 nm (for Hoechst 33342) or 647 nm (for Alexa Fluor™ 633) and appropriate settings for the used objective (NA 1.4; objective lens magnification 63×).

Segmentation and quantification: The IFITM3 signal of the deconvolved image stacks was segmented in 3 dimensions using the surface segmentation algorithm of Imaris (Verison 9.8.2, Oxford Instruments). The number of segmented objects per cell and the volume distribution of all objects were quantified.

Infection assay using wide-field fluorescent light microscopy

To analyze the antiviral effect of stable overexpression of IFITM3 in A549 cells, we performed an infection assay using the here established reporter virus A/WSN/1933-PA-mScarlet (see section above) as described below:

Viral infection: 5 × 10^4 A549 or A549-IFITM3 cells were seeded on 12 mm microscopy coverslips NO. 1 (Marienfeld) in a 24-well plate in complete growth medium (DMEM-F12, 10% FBS, 1% P/S). The next day, the cells were infected with a fluorescent report virus A/WSN/1933-PA-mScarlet using a MOI of 3 in serum free DMEM-F12 medium for 1 h at 37°C, 5% CO_2. Cells were washed 3 times with complete growth medium and incubated at 37°C, 5% CO_2. Cells were fixed 24 hpi with 4% PFA in PBS for 30 min at RT. After fixation, cells were washed 3 times with PBS.

Immunolabeling: Cells were permeabilized by incubation with 0.2% Triton X-100 in PBS for 5 min, followed by 3 washing steps with PBS for 5 min each. Cells were incubated for 1 h with blocking buffer (3% BSA in PBS supplemented with 0.1% PBS-T). After 3 short washing steps with PBS-T, cells were incubated for 1 h with primary antibody against M2 (Proteintech) using an antibody dilution of 1:50 in dilution buffer (1% BSA in PBS-T) at RT on a rocker. After 3 washing steps with PBS-T for 5 min each, cells were incubated with DAPI using a 1:1000 dilution (Sigma-Aldrich) and the secondary antibody 'goat anti-Mouse Alexa Fluor™ 633' (ThermoFisher Scientific, Invitrogen) in a dilution of 1,000 in dilution buffer for 1 h at RT on a rocker. Cells were washed 3 times with PBS for 5 min each, followed by a short washing step with deionized water. Coverslips were mounted on microscopy slides using 7 µl ProLong Glass Antifade mounting medium (ThermoFisher Scientific, Invitrogen). The mounting medium was cured for 24 h at RT.

Automated high-throughput fluorescent imaging: Wide field microscopy data was acquired using the Celldiscoverer 7 automated microscope (Zeiss) equipped with a 20×/0.95 NA PL APO COR objective and Axiocam 712 camera.

Quantification: Stitched composite images were binned 6 times in ImageJ/FIJI and nuclei were segmented using the StarDist plugin in ImageJ/FIJI (Schmidt et al., 2018). The average signal intensity in the segmented area of each individual nucleus was calculated for M1 and PA-mScarlet. Maximum average signal intensity for M1 and NP of non-infected control cells was determined and set as threshold to determine infected cells. Each nucleus with an average signal intensity for M1 ≤ 1,150 a.u. or PA ≤ 1,450 a.u. were counted as infected.

β-lactamase (Blam) membrane fusion assay

To analyze the impact of IFNβ treatment or IFITM3 overexpression in A549 cells on viral membrane fusion in late endosomes, we utilize a β-lactamase (Blam) based membrane fusion assay using influenza A virus-like particles (VLPs) expressing M1 with covalently bound Blam. Cells were laden with a fluorescence resonance energy transfer (FRET) substrate CCF4-AM (ThermoFisher Scientific, Invitrogen™), which can be proteolytically cleaved by Blam, resulting in an emission shift from 530 nm to 460 nm (Jones and Padilla-Parra, 2016), enabling the detection of cytoplasmic entry of M1-BlaM VLPs.

M1-Blam VLP production: 2.7 × 10^6 HEK293T cells were seeded in 10 ml complete growth medium (DMEM-GlutaMAX™-I, 10% FBS, 1% P/S) in a 10 cm cell culture dish. Cells were grown overnight at 37 °C and 5% CO_2. A transfection mix was prepared as follows: 1.48 µg pCAGGS-A/Hong Kong/1968-HA plasmid, 1.40 µg pCAGGS-A/Singapore/1957-NA, 7.12 µg pCAGGS-M1-Blam plasmid were added to a total volume of 1 ml Opti-MEM medium. 30 µl transfection reagent PEI (1 µg/µl, Polysciences) was added and incubated for 30 min at RT and added to the 10 cm dish with HEK293T cells. 6 h post transfection, cells were washed with PBS, and 10 ml OptiMEM medium supplemented with 1% P/S was added. After 48 h incubation at 37 °C and 5% CO_2, VLP-containing supernatant was harvested and centrifuged at 1,000 × g for 10 min to remove cell debris. 2.5 µl TPCK-Trypsin (10 µg/µl, Sigma-Aldrich) was added to the supernatant and incubated for 30 min at 37 °C to proteolytically cleave HA. TPCK-Trypsin was subsequently deactivated by adding 7 µl trypsin inhibitor (5 µg/µl in PBS, Sigma-Aldrich) and incubated for 10 min at 37 °C. VLP-containing supernatant was aliquoted, shock frozen in LN_2, and stored at -80 °C until further use.

Blam membrane fusion assay: For better cell attachment, a black-walled clear-bottom 96-well plate (Corning) was coated with fibronectin: 25 µl fibronectin solution (57.2 µg/ml fibronectin in PBS) was added to each well and incubated for 6 h at RT. The remaining solution was removed, and wells were washed 1 time with PBS. In each well, 1.2 × 10^4 A549 or A549-IFITM3 cells were seeded in 100 µl complete growth medium (DMEM-F12, 10% FBS, 1% P/S). The next day, A549 cells were treated with different concentrations of IFNβ (0, 100, 500, 1,000, 2,000 units/ml). After 48 h, cells were infected with 190 µl M1-Blam IAV-VLPs. Infection efficiency was enhanced by spinoculation with 250 × g for 1 h at RT. Cells were washed with PBS, and 90 µl Opti-MEM supplemented with 1% P/S and 20 mM HEPES was added to each well. Cells were incubated for 3 h at 37 °C and 5% CO_2. 20 µl of 6 µM CCF4-AM (ThermoFisher Scientific) in Blam loading solutions (ThermoFisher Scientific) was added to each well, and cells were incubated overnight at 8 °C on a cooling block.

Quantification with plate reader: Fluorescent signal was measured using the Infinite 200 plate reader (Tecan) with an excitation wavelength of 410 nm (9 nm bandwidth) and emission wavelengths of 450 nm or 520 nm (20 nm bandwidth) using a manual gain of 160 and 3 × 3 reads per well with an integration time of 20 µs and 50 reads per position. The background emission signal of medium only was subtracted from each measurement, and the ratio between the 450 nm and 520 nm emission signal was calculated. 450 nm / 520 nm ratios of replicates for each sample were averaged. Averaged ratios were normalized to the ratio of A549 cells and reported as relative membrane fusion inhibition between 0 and 1.

Fluorescent microscopy: After plate reader acquisition, representative images of each well were acquired using the Nikon Eclipse Ts2 fluorescent microscope equipped with a DS-Fi3 camera, 20× / 0.4 NA lens, and a custom filter cube optimized for Blam assay image acquisition.

Transmission electron tomography (ET)

To analyze the late endosomal morphology and quantify the number of ILVs, we performed ET on high pressure frozen and freeze-substituted (HPF/FS) cells. Section of cells were immuno-gold-labeled against IFITM3 to analyze the localization of IFITM3.

High pressure freezing (HPF): 2.8×10^5 A549 or A549-IFITM3 cells were seeded on carbon-coated 3 mm sapphire discs (Leica) in a 6-well plate in complete growth medium (DMEM-F12, 10% FBS, 1% P/S). A549 cells were treated with 2×10^3 units/ml IFNβ (Immuno Tools). After 24 h IFNβ treatment, cells were fixed by HPF: Carrier type A and B (Leica) were coated with 1-hexadecen. Excess 1-hexadecen was removed by blotting with a filter paper (Whatman, No. 1). The 100 µm deep inner groove of carrier A was filled with complete growth medium. The sapphire disc with cells was blotted on filter paper (Whatman, No. 1) and placed with the cells facing down on carrier A. Carrier B was placed with the flat site on top to close the sandwich. Sample was subsequently high-pressure frozen using an EM ICE HFP system (Leica).

Automated freeze substitution (AFS) and resin embedding: Lowicryl solution was prepared by adding 34.04 g monomer E, 5.96 g crosslinker D and 200 mg initiator C (Lowicryl HM20 resin kit, Polysciences Inc.). Freeze-substitution solution was prepared by solving 0.1 % uranyl acetate (UA) in acetone. All solutions and high-pressure frozen sapphire discs were loaded to the automated freeze substitution system AFS2 (Leica). A freeze substitution program was performed according to Table 1.

Table 1: Automated freeze substitution program.

Step	T start	T end	Slope	Time	Reagent	Transfer	Agitation	UV
1	-90°C	-90°C		48 h	0.1% UA	stay	off	off
2	-90°C	-45°C	5 °C/h	9 h	0.1% UA	stay	off	off
3	-45°C	-45°C		5 h	0.1% UA	stay	off	off
4	-45°C	-45°C		10 min	Acetone	exch/fill	off	off
5	-45°C	-45°C		10 min	Acetone	exch/fill	off	off
6	-45°C	-45°C		10 min	Acetone	exch/fill	off	off
7	-45°C	-45°C		4 h	10% Lowicryl	mix	on	off
8	-45°C	-45°C		4 h	25% Lowicryl	mix	on	off
9	-45°C	-35°C	2.5 °C/h	4 h	50% Lowicryl	mix	on	off
10	-35°C	-35°C	2.5 °C/h	4 h	75% Lowicryl	mix	on	off
11	-35°C	-35°C		10 h	100% Lowicryl	exch/fill	off	off
12	-35°C	-35°C		10 h	100% Lowicryl	exch/fill	off	off
13	-35°C	-35°C		10 h	100% Lowicryl	exch/fill	off	off
14	-35°C	-35°C		48 h	100% Lowicryl	stay	off	on
15	-35°C	20°C	5	9 h	100% Lowicryl	stay	off	on
16	20°C	20°C		48 h	100% Lowicryl	stay	off	on
17	20°C	20°C		72 h	100% Lowicryl	stay	off	off

Ultramicrotomy: Lowicryl embedded samples were trimmed and cut with a diamond knife (DiATOME) using a UC7 ultramicrotome (Leica) to obtain sections with 250 nm nominal thickness. Sections were placed on 2 × 1 mm copper slot grids (Gilder) with 1% formvar film, sputter-coated with 2 nm carbon using ACE600 sputter coater (Leica).

Immunolabeling: Sections were blocked for 30 min in blocking solution (PBS supplemented with 0.8% BSA and 0.1% FSG) and incubated for 1 h with the primary antibody against IFITM3 (Proteintech), using an antibody dilution of 1:5 in blocking buffer. Sections were washed 5 times for 5 min each with PBS. Samples were incubated for 1 h with 10 nm Protein-A Gold (PAG) (Aurion) diluted 1:50 in blocking buffer. Sections were washed 5 times for 5 min each with PBS and subsequently 5 times for 2 min in H_2O.

Tilt series acquisition: Tilt series were acquired on a 300 keV transmission electron microscope (TEM) Tecnai F30 (FEI), equipped with a Gatan OneView 4K camera, from +60° to -60° tilt with 1° steps using a pixel spacing of 1.03 nm using the SerialEM software (Mastronarde, 2005).

Segmentation and quantification: Tomograms were reconstructed in batch with patch tracking and R-weighted back projection using the IMOD software package (Kremer et al., 1996). To remove bias in data analysis, a de-identified dataset was created. All late endosomes in the reconstructed tomograms were segmented in Three-dimensions using the IMOD software package (Kremer et al., 1996). Every 10 section, the endosome was manually segmented using the sculpt drawing tool. Segmented sections were interpolated to generate a volume.

Volume segmentation was meshed and total volume inside the mesh was calculated. The number of ILVs were manually counted for each late endosome. The ILV density was calculated for each late endosome by dividing the number of ILVs with the volume of the late endosome.

Cholesterol-analog cross-linking and immunoprecipitation

A549-IFITM3 cells were seeded in 10 cm cell culture dishes at a density of 4×10^6 cells per dish in complete growth medium (DMEM-F12, 10% FBS, 1% P/S). After 24 h, cells were labeled with a photo-reactive and clickable cholesterol analog (pacChol) (Sigma-Aldrich) with a final concentration of 6 µM for 30 min at 37 °C and 5% CO_2. As a control, 0.096 v/v% DMSO was used. After 2 washing steps with phosphate-buffered saline (PBS) supplemented with 1mM $MgCl_2$ and 0.1 mM $CaCl_2$, UV crosslinking was performed using the BIO-SUN device (Vilber Lourmant) with 5 J/cm^2 for 20 min. Cells were lysed using 500 µl lysis buffer (PBS with 1% Triton X-100, 0.1% SDS, 2× protease inhibitor cocktail, 0.125 units/µl benzonase) per 10 cm dish for 1 h at 4 °C on a rotary wheel. The lysate was centrifuged for 15 min at 4 °C with 16,000 × g. 39 µl Biotin click reaction working solution (1,000 µM $CuSO_4$, 100 µM Biotin-azide, 1,000 µM TCEP, 100 µM TBTA) was added to 500 µl of lysate supernatant and incubated for 3 h at 37 °C on a shaker with 1,000 rpm. Click-reaction was stopped by adding 4 ml of ice-cold methanol. The sample was centrifuged for 20 min at 4 °C with 3,000 × g. The supernatant was discarded, and the pellet was washed 2 times with ice-cold methanol and subsequently air-dried. Pellet was resuspended in 15 µl of 4% SDS in PBS and dissolved by sonication. The sample was diluted 1:40 in PBS with 1% Triton X-100 for further analysis. 20 µl high capacity NeutrAvidin (Sigma-Aldrich) agarose beads were added to 600 µl sample and incubated overnight at 4 °C. The sample was centrifuged for 3 min at 4 °C with 3,000 × g. Beads were washed 3 times with PBS supplemented with 1% Triton X-100. The sample was eluted with 20 µl Laemmli buffer and further analyzed by immunoblotting using anti-IFITM3 (1:2,000) and anti-Caveolin1 (1:1,000) antibodies on a pre-cast 10 – 20% Tricine gel (ThermoFisher Scientific). The 'Precision Plus' (Bio-Rad) prestained protein size marker was used.

Molecular dynamics simulations

The initial IFITM3 structure (residues 59 – 133) and its orientation in the membrane was kindly provided by Emma H. Garst (Garst et al., 2021). IFITM3 was inserted into model membranes using the CHARMM-GUI Membrane Builder web interface (Lee et al., 2016, 2019). First, the palmitoyl group was added at Cys72 during the membrane builder system building

process. Next, several potassium or chloride atoms were added to neutralize the systems. Finally, KCl salt at a concentration of 150 mM was added to mimic the intracellular environment. Protein, lipids, and salt ions were described using the CHARMM36m force field (Huang and MacKerell, 2013; Huang et al., 2017; Pastor and Mackerell, 2011). For water, we used the TIP3 model (Jorgensen et al., 1983).

Equilibration of the systems was conducted with CHARMM-GUI standard protocol. Briefly, all the systems were subjected to energy minimization using the steepest descent algorithm. After minimization, we ran six steps of equilibration runs where we gradually reduced the force constant applied to restrain the positions of the protein and the lipids. For the production run, we employed the Parrinello-Rahman barostat (Parrinello and Rahman, 1981) with a semi-isotropic pressure coupling scheme and a time constant set to 5.0 ps to maintain the pressure constant. The pressure was set to 1.0 bar and the isothermal compressibility to 4.5×10^{-5} bar^{-1}. The temperature was maintained at 310 K using the Nose-Hoover thermostat (Hoover, 1985; Nosé, 1984) with a time constant of 1.0 ps. Electrostatic interactions were handled using the PME method (Darden et al., 1993; Essmann et al., 1995). The cut-off length of 1.2 nm was used for electrostatic (real space component) and van der Waals interactions. Hydrogen bonds were constrained using the LINCS algorithm (Hess et al., 1997). Finally, periodic boundary conditions were applied in all directions. The simulations were carried out using an integration time step of 2 fs with coordinates saved every 100 ps. All systems were simulated for 1 microsecond with the GROMACS-2021 software (Abraham et al., 2015). The images were rendered using VMD (Humphrey et al., 1996).

Late Endosomal Membrane: The evaluation of the lipid composition in the late endosome is highly inaccurate and should be considered a rough estimation since the lipid composition changes as the endosome matures. Moreover, the ILVs and the limiting membrane have different lipid compositions (Huotari and Helenius, 2011). The cholesterol/phospholipids ratio decreases from 1/1 ratio at the early endosome to 1/2 in the late (Van Meer et al., 2008). The major phospholipids head groups in the late endosome are (Kobayashi et al., 2002) phosphatidylcholine (PC) 48.2%, phosphatidylethanolamine (PE) 19.8%, lysobisphosphatidic acid (LBPA) 15.7%, Sphingomyelin (SPH) 9.2%, phosphatidylinositol (PI) 4.1% and phosphatidylserine (PS): 2.4%. The lipid tails saturation is unknown in the late endosome, so we estimate it based on the known values in the plasma membrane (Lorent et al., 2020). The majority of LBPA tails, which is not present in the plasma membrane, are 18:1 (~ 92%) (Kobayashi et al., 2002). Finally, the percentage of lysolipids (excluding LBPA) is about 4 –

5% in all the cell organelles examined (Zambrano et al., 1975). The used late endosomal-like lipid composition used for MD simulation is summarized in Table 2.

Table 2. Complex lipid composition mimicking the late endosomal membrane

Abbreviation	Full name	Mole percent	Intrinsic curvature	References for intrinsic curvature
POPC	1-palmitoyl-2-oleoyl-sn-glycero-3-phosphocholine	35.1	-0.02	Kollmitzer et al., 2013
POPE	1-palmitoyl-2-oleoyl-sn-glycero-3-phosphoethanolamine	7.3	-0.32	Kollmitzer et al., 2013
DOPE	1,2-dioleoyl-sn-glycero-3-phosphoethanolamine	7.3	-0.35	Fuller and Rand, 2001
PSM	Palmitoylsphingomyelin	5.3	-0.13	Kollmitzer et al., 2013
LBPA	Lysobisphosphatidic acid	9.9	Negative, exact value unknown	Kobayashi et al., 2002
CHOL	Cholesterol	29.8	-0.5	Kollmitzer et al., 2013
LPC16	Lysophosphatidylcholine	4.0	0.15	Fuller and Rand, 2001
LPE16	Lysophosphatidylethanolamine	1.3	0.03	Fuller and Rand, 2001

Enrichment/Depletion analysis: For enrichment/depletion analysis, we calculate the number of lipids (for each lipid type) within a radial cut-off distance of 0.4. In addition, the molar fractions of lipids surrounding IFITM3 have been calculated with respect to the lipid bulk concentrations (lipids above the radial cut-off distances). The analysis was carried out employing the 'gmx select' and in-house python scripts. The first 20 ns have been considered as equilibration time and then excluded from the analysis. The standard deviation is reported in the error bar with n = 3.

Normalized contact occupancy: Over time, the number of contacts has been calculated using the 'gmx mindist' GROMACS analysis tool. A contact is defined if the distance between any atoms of IFITM3 and POPC (or cholesterol) is less than 0.4 nm. Data are normalized based on the total number of lipids of each lipid type. The first 200 ns have been considered as equilibration time and then excluded from the analysis. The error bar is shown as the standard deviation.

Relative affinity and repulsion of lipid to IFITM3

We calculate the relative affinity and repulsion of different lipid species to IFITM3 by considering the two competing forces governing the lipid distribution – the direct interaction between lipid to IFITM3 and the demixing entropy that resists it. To do so, we use the following assumptions: Each monolayer is composed of M number of different lipid species, and each lipid species has n_j lipids in each monolayer. No lipid flip-flop was observed during the MD simulations, and therefore, we prohibit it in the following derivation. We define two regions in

each monolayer – the immediate vicinity of the IFITM3 (Figure 2B, green) and the bulk (Figure 2B, orange), given by the superscripts b (bound) and f (free), respectively. Lipids can freely diffuse between the regions, but since the lipids are closely packed and have a high stretching-compression modulus, we assume their density and number in each region are fixed, N^b and N^f, respectively. Therefore, the free energy can only be relaxed by lipid exchange between the bound and free regions, Δn_j, which must satisfy the following requirement:

$$\sum_{j=1}^{j=M} \Delta n_j = 0. \tag{1}$$

The total free energy that is associated with the lipid's interaction energy with IFITM3 and mixing entropy is given by

$$F = \sum_{j=1}^{j=M} \left[n_j^b \left(u_j + k_B T \cdot \ln \frac{n_j^b}{N^b} \right) + k_B T \cdot n_i^f \cdot \ln \frac{n_i^f}{N^f} \right]. \tag{2}$$

To find the equilibrium distribution, one must minimize Equation 2 with respect to Δn_j while maintaining the constraint of a fixed number of lipids and Equation 1, which can be done numerically. However, MD simulations found that most lipid exchange is due to cholesterol repulsion from IFITM3. Therefore, we consider cholesterol exchange with all of the other lipids combined. With that, Equation 2 is minimized by allowing only the exchange of Δn cholesterols with any other lipid. The relative repulstion of cholesterol is given by

$$\Delta u = u_{Chol} - u_0 = k_B T \ln \left[\frac{n_{Chol}^f}{n_{Chol}^b} \cdot \frac{N^B - n_{Chol}^b}{N^f - n_{Chol}^f} \right] \tag{3}$$

with $n_{chol}^{b,f}$ and $N^{b,f}$ the number of cholesterol and the total number of lipids in the free or bound areas (donated by the super-script b or f), respectively. u_0 is the averaged interaction energy of IFITM3 with all other lipids except cholesterol and u_{chol} is the interaction energy with cholesterol. This procedure is performed separately on the luminal and cytosolic facing and monolayers to find the relative repulsion of each, Δu_l and Δu_c, respectively. We also performed this procedure on the two monolayers combined to find the relative repulsion of cholesterol to IFITM3 in the membrane.

Modeling of membrane fusion and lipid sorting

Membrane elasticity theory: We use a continuum approach based on lipid tilt and splay theory to model the lipid deformations in the hemifusion diaphragm and its vicinity. Previous works present the theory and related computations in detail (Akimov et al., 2020; Golani et al., 2021; Kozlovsky et al., 2002). In short, the hemifusion diaphragm is modeled as a membrane

surrounded by the virus and endosome membranes, and the diaphragm rim represents the merger of the three (Figure 6A). Each membrane comprises two lipid monolayers that contact along a joint mid-plane. The deformation of the lipids in each monolayer is described by their tilt, splay, and saddle-splay (Hamm and Kozlov, 2000; Helfrich, 1973). All are defined with respect to the monolayer dividing plane. Here we take the distance from the membrane mid-plane to the monolayer dividing plane to be $\delta = 1.5\,\mathrm{nm}$ (Kozlov and Winterhalter, 1991) and explicitly assume that they are parallel.

Lipid tilt deformation is generated due to the shearing of the hydrocarbon tails in the vicinity of the diaphragm rim. It is defined as $\vec{t} = \frac{\vec{n}}{\vec{n}\cdot\vec{N}} - \vec{N}$, with $\vec{n}$ the lipid director and $\vec{N}$ the normal to monolayer dividing plane (Hamm and Kozlov, 2000), as presented in Figure 3C. Splay deformations originate from the curvature deformations and the lateral change of the lipid tilt (Hamm and Kozlov, 1998, 2000). Mathematically, the lipid splay tensor is defined as the covariant derivative of the lipid director, $\tilde{b}_{\alpha}^{\beta} = \nabla_{\alpha} n^{\beta}$, where the sub- and superscripts denote, respectively, the co- and contravariant components in the local coordinate basis of the monolayer dividing plane and (Hamm and Kozlov, 2000). Lipid splay is the trace of the splay tensor, defined as $\tilde{J} = \tilde{b}_{\alpha}^{\alpha}$, where the summation is performed over repeating indices. In the absence of tilt, lipid splay has the meaning of the sum principal curvatures, c_1 and c_2, referred to as total curvature, $J = c_1 + c_2$. Similarly, lipid saddle-splay is a generalization of Gaussian curvature, $K = c_1 \cdot c_2$, in the presence of both bending and tilt deformations. In co-contra variant form, it is the determinant of the splay tensor, $\tilde{K} = \det \tilde{b}_{\alpha}^{\beta}$ (Hamm and Kozlov, 2000b). The elastic energy density is given by (Hamm and Kozlov, 2000)

$$f_m = \frac{1}{2}\kappa_m(\tilde{J}^2 - 2\tilde{J}J_{sm}) + \bar{\kappa}_m\tilde{K} + \frac{1}{2}\kappa_t\vec{t}^2 \tag{4}$$

with κ_m , κ_t and $\bar{\kappa}_m$ the monolayer's bending, tilt, and saddle-splay rigidities, respectively. Their values are estimated from the literature to be 14.4 k_BT (Dimova, 2014), -7.2 k_BT (Templer et al., 1998; Terzi et al., 2019), and 40 mN/m (Doktorova et al., 2017; May et al., 2004), respectively. The spontaneous monolayer curvature, J_{sm}, is determined by the monolayer constituting lipids and proteins intrinsic curvatures, ζ_j, and their relative mol fractions, ϕ_j. With j being index representing the different components. The overall spontaneous monolayer curvature is the sum of its components (Kollmitzer et al., 2013; Kozlov and Helfrich, 1992; Safran et al., 1990)

$$J_{sm} = \sum \zeta_j \phi_j. \tag{5}$$

However, since IFITM3 is strongly repelling cholesterol, we consider the membrane to be composed of just two lipid subgroups – cholesterol with intrinsic curvature of $\zeta_{chol} = -0.5\ \mathrm{nm}^{-1}$ (Table 2) and all of the other lipid species grouped have the mean intrinsic curvature of $\zeta_0 = -0.1\ \mathrm{nm}^{-1}$ (Table 2), we term the second group 'background' lipids. The overall elastic energy is found by integrating the energy density in Equation 4 over the area of the monolayers

$$U_E = \int_{all} f_m dA - U_e^{pre}. \tag{6}$$

The elastic energy is with respect to the pre-fusion configuration of two flat non-interacting membranes, U_e^{pre}. The equilibrium shape of the fusion site is found by minimizing Equation 6 as will be explained in the section 'Numerical computation of fusion site shape and fusion pore energy barrier'.

IFITM3 induced lipid sorting: In addition to lipids, the endosomal membrane contains uniformly distributed IFITM3 proteins that repel cholesterol and attract other lipids instead. The virus and diaphragm membranes do not contain IFITM3 because the diaphragm rim acts as a semi-permeable barrier that allows only lipids to pass. The formation of the IFITM3-free region allows the system to relax some of the relative repulsion energy between cholesterol and IFITM3 at the cost of entropic demixing energy.

To calculate the magnitude of exchange, we consider two membrane domains with a total of N lipids. One domain represents all the lipids that are closely bound to IFITM3 with $N^b = N_{IFITM3} \cdot n_{inter}$ lipids, N_{IFITM3} is the total number of IFITM3 proteins in the endosome and n_{inter} the number of lipids interacting with each, as found in MD simulations ($n_{IFITM3} = 52$ was used in all simulations as it is the value found in the 'realistic composition'). The second domain contains the remaining lipids $N^f = N - N^b = N - N_{IFITM3} \cdot n_{inter}$. As explained above, we consider two subgroups of lipids: N_{chol} cholesterols lipids and $N_0 = N - N_{chol}$ background lipids. The relative repulsion of the two to IFITM3 is $\Delta u = u_{Chol} - u_0$. The number of cholesterol lipids is n_{chol}^f and the number of background lipids is $n_0^f = N^f - n_{chol}^f = N - N_{IFITM3} \cdot n_{inter} - n_{chol}^f$ in the free domain. The lipid numbers in the bound domain are $n_{chol}^b = N_{chol} - n_{chol}^f$ and $n_0^b = N^b - n_{chol}^b = N_{IFITM3} \cdot n_{inter} - N_{chol} + n_{chol}^f$. To find the equilibrium distribution, one can use a similar procedure leading to Equation 3 to have

$$\Delta u = k_B T \ln\left[\frac{n_{Chol}^f}{N_{chol} - n_{chol}^f} \cdot \frac{N_{IFITM3} \cdot n_{inter} - N_{chol} + n_{chol}^f}{N - N_{IFITM3} \cdot n_{inter} - n_{chol}^f}\right]. \tag{7}$$

We define the mole fractions: $\phi_{IFITM3} = N_{IFITM3}/N$, $\phi_{chol} = N_{chol}/N$, and $\phi_{Chol}^{f} = n_{Chol}^{f}/N^{f} = n_{Chol}^{f}/(N - N_{IFITM3} \cdot n_{inter})$ and rewrite Equation 7 as

$$\Delta u = k_B T \ln\left[\frac{\phi_{Chol}^{f}}{1-\phi_{Chol}^{f}} \cdot \frac{\phi_{IFITM3} \cdot n_{inter} - \phi_{chol} + \phi_{Chol}^{f}(1-\phi_{IFITM3} \cdot n_{inter})}{\phi_{chol} - \phi_{Chol}^{f}(1-\phi_{IFITM3} \cdot n_{inter})}\right]. \quad (8)$$

The total cholesterol mole fraction is estimated based on the known literature to be $\phi_{chol} = 0.3$ in the late endosome (Van Meer et al., 2008), Δu is found based on the MD simulation as described above and ϕ_{IFITM3} is the free parameter of the model. We find ϕ_{Chol}^{f} by rearranging Equation 8 and solving the quadratic equation

$$\phi_{Chol}^{f}{}^{2}(1 - \phi_{IFITM3} \cdot n_{inter})\left(1 - e^{-\frac{\Delta u}{k_B T}}\right) - \phi_{Chol}^{f}\left[1 - \phi_{IFITM3} \cdot n_{inter}\left(1 - e^{-\frac{\Delta u}{k_B T}}\right) + \phi_{chol}\left(1 - e^{-\frac{\Delta u}{k_B T}}\right)\right] + \phi_{chol} = 0. \quad (9)$$

The magnitude of lipid exchange is defined as the change of cholesterol level from the baseline levels with no IFITM3 in the endosome $\Delta\phi = \phi_{Chol}^{f} - \phi_{chol}$.

Next, we derive the spontaneous curvature in the endosome, virus, and diaphragm monolayers. Since the relative affinities of lipids to IFITM3 are similar on the luminal and cytosolic sides, we consider the magnitude of the lipid exchange to be the same in both leaflets. In addition, because the typical time in hemifusion is in the order of minutes while the flip-flop time of cholesterol is measured in milliseconds, we also assume the system to be in equilibrium with respect to lipid flip-flop.

The virus and hemifusion diaphragm have the lipid composition of the 'free' domain, their monolayer spontaneous-curvature is (Equation 5)

$$J_{sm}^{v,d} = \left(1 - \phi_{Chol}^{f}\right)\zeta_0 + \phi_{Chol}^{f}\zeta_{chol}. \quad (10)$$

The endosomal membrane contains patches of both free and bound domains since IFITM3 proteins are dispersed in it. However, since the IFITM3 proteins freely diffuse and are uniformly distributed, the lipids are also uniformly distributed on time-average. So although IFITM3 triggers a local change in lipid composition in its immediate vicinity (< 1 nm), we treat the endosomal membrane as a smooth continuum and average other these spatial fluctuations. Moreover, we also consider the endosomal membrane much larger than the virus, so the enrichment of cholesterol in the virus has a negligible effect on the cholesterol mole fraction in the endsome. Lastly, we account for possible intrinsic curvature of the amphipathic helix domain of IFITM3 that was recently reported (Guo et al., 2021) in the 'with sorting and curvature' and 'no sorting; with curvature' scenarios. Specifically, we attribute

the intrinsic curvature of $\zeta_{IFITM}^{c} = -0.62\,\mathrm{nm}^{-1}$ to the cytosolic side because there the amphipathic helices are located. Given all of that, the endosome cytosolic facing monolayer spontaneous-curvature is (Equation 5)

$$J_{sm}^{c,endo} = \zeta_0(1 - \phi_{chol} - \phi_{IFITM3}) + \zeta_{chol}\phi_{chol} + \zeta_{IFITM3}\phi_{IFITM3}. \tag{11}$$

Here we also assumed for simplicity that the amphipathic helix domain has the same projected size as a lipid. The luminal facing side of IFITM3 contains a transmembrane domain, which to our knowledge, does induce any curvature. Therefore, the endosome luminal-facing monolayer spontaneous curvature is (Equation 5)

$$J_{sm}^{l,endo} = \zeta_0(1 - \phi_{chol} - \phi_{IFITM3}) + \zeta_{chol}\phi_{chol}. \tag{12}$$

In the 'with sorting; no curvature' scenario, we set $\zeta_{IFITM3} = 0$. We also tested the possibility that the amphipathic helices of IFITM3 penetrate the diaphragm in such a case, there is no sorting. The monolayer spontaneous-curvature of the diaphragm cytosolic facing monolayer is equivalent to that of the endosomal one.

Pore Expansion energy barrier and first passage time

The magnitude of fusion-pore formation energy barrier: A membrane pore must open and expand in the hemifusion diaphragm to complete the fusion reaction (Akimov et al., 2017; Weaver and Chizmadzhev, 1996). The driving force for fusion pore expansion is the removal of lipids from the highly stressed region in the diaphragm and their migration to the more relaxed surrounding membrane. The energy gained by this process is given by

$$U_{removal} = \int \left(f_{Dia}^{l} + f_{Dia}^{c}\right) \cdot dA \tag{13}$$

with f_{Dia} being the position-dependent energy density in the diaphragm monolayers (Equation 4). The superscripts l and c represent the diaphragm luminal and cytosolic facing monolayers, respectively. The integral in Equation 13 is done over the pore area of size A. The fusion pore expansion is resisted by the energetic cost of forming the pore rim, $U_{pore\,rim} = \lambda L$, with λ to pore rim line tension and L the pore rim length. The line tension depends strongly on the lipid composition. In a two lipid component system, the effect of the relative mol fraction change, $\Delta\phi$, is given by (Chernomordik et al., 1985)

$$\lambda = \lambda_0 - \pi\kappa_m(\zeta_{chol} - \zeta_0)\Delta\phi. \tag{14}$$

The first term in Equation 14, λ_0, accounts for the contribution to line tension independent of change in lipid composition. It includes all the other lipid deformations in the pore rim. Its value is estimated as $\lambda_0 = 15$ pN for a membrane containing 30% cholesterol based on theoretical considerations (Akimov et al., 2017) and experiments (Portet and Dimova, 2010). The energy needed for pore expansion is the sum of the energy cost of creating the pore rim and the energy gained by the removal of lipids (Equations 13 and 14)

$$E_{pore} = U_{pore\,rim} - U_{removal}. \tag{15}$$

The pore opening energy, E_{pore}, is characterized by the critical pore radius, ρ^*, smaller pores tend to close while larger tend to expand infinitely (Figure 3E). The energy of pore expansion at the critical size is the pore expansion energy barrier,

$$E^* = \max\left[E_{pore}\right]. \tag{16}$$

Dwell time in hemifusion: Thermal fluctuations determine the dynamics of the pore size; small pores flicker in size until they eventually reach the critical size beyond which they irreversibly expand (Chanturiya et al., 1997). The mean time needed for the pore size to cross the energy barrier was already described in detail in earlier works, primarily for uniformly stressed membranes (Taupin et al., 1975) but also in the specific case of pores in the hemifusion diaphragm (Golani et al., 2021)

$$\tau = \tilde{\tau} \cdot e^{\frac{E^*}{k_B T}} \tag{17}$$

with $\tilde{\tau}$ being a pre-exponent factor that depends on an unknown microscopic time constant. We evaluate the efficiency of IFITM3 in inhibiting fusion by calculating the ratio between the typical time for pore expansion with and without IFITM3, τ_{IFITM3} and τ_0 respectively

$$\beta = \frac{\tau_{IFITM3}}{\tau_0} = \exp\left(\frac{E^*_{IFITM3} - E^*_0}{k_B T}\right). \tag{18}$$

Here we assume that $\tilde{\tau}$ is unchanged by slight changes in lipid composition and that the change in the diaphragm area available for fusion is negligible. We term β as the 'inhibition factor' and the difference in pore expansion energy barrier due to IFITM3 presence as $\Delta E^* = E^*_{IFITM3} - E^*_0$.

Numerical computation: Our computation aims to estimate the inhibition factor of IFITM3. The computation is divided into two steps. First, we calculate the equilibrium shape of the

hemifusion diaphragm by minimizing Equation 6 using an iterative approach. The membranes' mid-planes and tilt angles are gradually changed until minimal energy configuration is found. The geometry of the fusion site is described by the junction angles (Figure 3A), φ_v and φ_c, the diaphragm size R_D, fusion site size at the virus and endosome sides R_r^{endo} and R_r^v, and distance between virus and endosome, h, is also subjected to energy minimization. The process is repeated from different initial configurations to ensure that minimal energy is genuinely found.

Next, based on the resulting equilibrium configuration and the adjusted lipid composition in the diaphragm, we calculate the energy barrier of pore expansion, ΔE^*, (Equation 16), and the inhibition factor β (Equation 18). The pore is more likely to initially form close to the diaphragm rim, where the stress is maximal. However, our computations show that the critical pore size is comparable to the size of the diaphragm, making the energy barrier mostly independent of the starting position. Therefore, to facilitate the computations, we assume that the fusion pore growth starts at the center of the diaphragm and radially expands. We also assume that the diaphragm's shape is unaffected by the growth of the pore. All computations are done using self-written MATLAB code, which is available on GitHub (https://github.com/GonenGolani/Fusion_Solver).

In situ **cryo-correlative light and electron microscopy (cryo-CLEM)**

In situ cryo-CLEM was performed on cryo-FIB milled samples based on a previously established method (Klein et al., 2021a, 2021b), as described below:

Sample preparation: 1.8 × 10^5 A549 or A549-IFITM3 cells were seeded on glow-discharged 200 mesh gold grids with a holey SiO_2 film with R1/4 spacing (Quantifoil) placed in a 35 mm dish and cultured in 2 ml complete growth medium (DMEM-F12, 10% FBS, 1% P/S). To facilitate grid handling, the 35 mm dish was coated with polydimethylsiloxane Sylgard 184 (Dow Corning) as described in Klein et al., 2021a. The next day, cells were infected with fluorescently labeled IAV (A/WSN/1933-nDiO) using a MOI of 200. Virus stock was diluted to a final concentration of 5 × 10^6 PFU/ml in infection medium (DMEM-F12, 20 mM HEPES). EM grids were blotted on filter paper (Whatman No. 1) and placed on Parafilm. 20 µl of the virus dilution was added on the grid and incubated for 30 min at 12 °C on a cooling plate to allow viral cell attachment. EM grid was washed 5 times with infection medium and was subsequently incubated for 1 h at 37 °C, 5% CO_2 in complete growth medium, supplemented with 100 nM Lipi-Blue (Dojindo) to fluorescently label lipid droplets. 1 hpi, infected cells were washed 2 times with complete growth medium, grids were manually blotted on filter paper

(Whatman No. 1) and a defined volume of 3 µl complete medium was added to the grid to ensure identical blotting conditions. Grid was subsequently blotted and vitrified by plunge freezing in liquid ethane using the EM GP2 automated plunge freezing device (Leica) using the following settings: 70% air humidity, 25 °C air temperature, -183 °C ethane temperature, 3.5 sec blotting from the back using a filter paper (Whatman No. 1).

Cryo-light microscopy (cryo-LM): Fluorescent signal of the plunge frozen samples were acquired on the cryoCLEM wide-field microscope (Leica Microsystems) (Schorb et al., 2017) equipped with a 50x/0.9 NA objective. A 1.2 × 1.2 mm area of the center of each grid was mapped, acquiring a volume stack of 30 µm thickness with a Z-spacing of 300 nm using the LAS X Navigator software (Leica). Image stacks were deconvolved with AutoQuant X3 (Media Cybernetics) using a theoretical and adaptive point spread function (PSF) for 100 iterations with the following parameters: lens immersion refractive index 1; sample embedding refractive index 1.31; sample distance from coverslip of 0 nm; emission wavelength of 460 nm (for Lipi-Blue) or 525 nm (for nDiO) and appropriate settings for the used objective (NA 0.9; objective lens magnification 50x). For cryo-correlative light and electron microscopy (cryo-CLEM), lamellae were mapped again by cryo-LM after cryo-TEM and correlated with the cryo-TEM map of the lamella using the post-correlation cryo-CLEM toolbox (Klein et al., 2021a).

Cryo-focused ion beam milling (cryo-FIB): Samples were mapped by cryo-scanning electron microscopy (cryo-SEM) on an Aquilos dual-beam cryo-focused ion beam-scanning electron microscope (cryo-FIB-SEM) (Thermo Fisher Scientific) with a cryo-stage cooled to -180 °C. The cryo-LM map of the grid was correlated to the cryo-SEM map using the MAPS Software (Thermo Fisher Scientific) (Schorb and Sieckmann, 2017). Infected cells were selected for milling. A protective organo-metallic platinum layer was applied for 5 sec to the grid and cells were milled gradually in 5 steps with a stage angle between 15° and 18° using a Gallium ion beam (Wagner et al., 2020). The nominal thickness of the milled lamella at the last milling step was 150 nm. Micro-expansion joints milling pattern were used to minimize lamella bending (Wolff et al., 2019).

Cryo-electron tomography (cryo-ET): Cryo-ET data was acquired on a Krios cryo-TEM (Thermo Fisher Scientific) operated at 300 keV equipped with a K3 direct electron detector (Gatan) and Quanta Gatan Imaging Filter (Gatan) with an energy slit set to 20 eV. Lamellae were mapped using SerialEM (Mastronarde, 2005) at 8,700× (pixel spacing of 10.64 Å) using a defocus of -50 µm to localize multivesicular organelles which were selected for acquisition. Tilt series were acquired with SerialEM (Mastronarde, 2005) using a dose-symmetric tilting

scheme (Hagen et al., 2017) with the zero angle set to 8° and a nominal tilt range of 68° to -52° with 3° increments using the following settings: Target focus of -3 µm, electron dose per record of 3 $e^-/Å^2$ and a magnification of 33,000× (pixel spacing of 2.67 Å).

Tomogram reconstruction: Frames were split into even and odd and subsets were aligned using Motioncor2 (Zheng et al., 2017). Even and odd datasets were reconstructed in parallel with identical setting in etomo as part of the IMOD software package (Kremer et al., 1996) using patch tracking for tilt series alignment. CTF estimation and 3D CTF-correction was performed in etomo. Tomogram was reconstructed using weighted back-projection with a simultaneous iterative reconstruction technique (SIRT)-like filter equivalent to 5 iterations and dose-weighting filter. Using the reconstructed tomograms from the even and odd datasets, data was denoised using a Noise2Noise algorithm implemented in the CryoCare software package (Buchholz et al., 2019) on non-binned data.

Volume rendering: The reconstructed and denoised tomogram volume was segmented in 3 dimensions using the Amira software (Thermo Fisher Scientific). First, a non-local means and membrane enhancement filter was applied. Membranes were automatically segmented using the Top-hat tool. The segmentation was manually refined by removing segmentation derived by noise. In addition, missing parts of the limiting late endosomal membrane, ILVs and the viral membranes were manually added. The number of direct interactions between the viral particles and ILVs or the limiting late endosomal membrane were quantified.

Analysis of hemifusion symmetry: For each hemifusion site at the limiting late endosomal membrane or at ILVs in the endosomal lumen the length of the hemifusion diaphragm and the inner and outer angles (as defined in Figure4A) were measured. The tomogram was resliced using the slicer tool in IMOD (Kremer et al., 1996) to position the hemifusion site on a single X-Y plane. All individual angles were measured using the 'angle tool' in ImageJ/FIJI (Schindelin et al., 2012). To measure the hemifusion diaphragm length, a line profile with 10 px width was plotted. The average signal of the late endosomal lumen was subtracted. The difference between the zero-crossing points was determined and reported as the diaphragm length. Thus, the measurement includes the phospholipid monolayers.

Estimation of pore formation energy barrier based on cryo-EM data

We use the theory described above to estimate the magnitude of the fusion-pore formation energy barrier based on the cryo-EM data. The stress in the diaphragm depends only on the geometry of the fusion site and specifically on the tilt magnitude at its rim, given by

$$t_0 = \tan\left[\frac{\pi-\varphi}{2}\right] \tag{19}$$

With φ the inner angle of the fusion site either and the virus or cytoplasmic side (Figure 5A). Since we assume that the diaphragm is axially symmetric and no significant differences were observed between opposing angles, we take the inner angle as the average $\varphi_c = \frac{c+c\prime}{2}$ and $\varphi_v = \frac{b+b\prime}{2}$ (Figure 5B). The lipid tilt propagates towards the center of the diaphragm and vanishes at its center. The tilt radial dependence can be approximated to (Golani et al., 2021)

$$\vec{t}(\rho) = -t_0 \frac{\mathrm{I}_1(l^{-1}\rho)}{\mathrm{I}_1(l^{-1}R_D)}\hat{\rho} \tag{20}$$

With $\mathrm{I_n}$ the modified Bessel functions of the first kind, ρ the radial coordinate, $l = \sqrt{\frac{\kappa_m}{\kappa_t}} = 1.2\ \mathrm{nm}$ the tilt decay length. The diaphragm mid-plane radius, R_D, is related to the measured diaphragm diameter (Figure 5C) by $R_D = \frac{g-L}{2}$. With L the membrane thickness measured from headgroups to headgroups of opposing monolayers and g the distance between head groups at the diaphragm rim. We take L to be 6 nm based on our cryo-EM data. The change in tilt induces lipid splay, and saddle-splay is given by (Golani et al., 2021)

$$\tilde{J} = -\frac{t_0}{2l\mathrm{I}_1(l^{-1}R_D)}\left[\mathrm{I}_0(l^{-1}\rho) + 2\frac{l}{r}\mathrm{I}_1(l^{-1}\rho) + \mathrm{I}_2(l^{-1}\rho)\right] \tag{21}$$

$$\widetilde{K} = \frac{t}{r}\frac{\partial t}{\partial r} = \frac{t_0^2}{2rl}\frac{\mathrm{I}_1(l^{-1}r)}{\mathrm{I}_1^2(l^{-1}R_D)}\left[\mathrm{I}_2(l^{-1}\rho) + \mathrm{I}_0(l^{-1}\rho)\right] \tag{22}$$

We use Equations 20-23 to calculate the tilt, splay, and saddle-splay in each monolayer separately and the membrane stress using Equation 4. Finally, each fusion site's pore formation energy barrier is calculated using Equation 16.

Subtomogram averaging (STA)

To characterize the state of the influenza A fusion protein HA, which was regularly found at the hemifusion sites, we performed subtomogram averaging. In total, 30 individual putative HA densities at hemifusion sites were identified and extracted using a dipole model in Dynamo (Castaño-Díez et al., 2012) using a box size of 192 pixel (equals 51.28 nm). An initial reference model was created by averaging all subvolumes with the orientations extracted by the dipole model. Azymuth angles were randomized to evenly distribute the missing wedge of the individual subvolumes during initial model creation. The first averaging was calculated without symmetry operation (C1) using a spherical mask (Figure S13A). The used numerical

parameters for the STA calculation are listed in Table 3. The resulting average of the first STA was used as new template for the second average, using a tight mask around the central density corresponding to the HA. In the second average a C3 symmetry operation was applied (Figure S13B) and the same numerical parameters were used (Table 3).

Table 3. Numerical parameters for STA calculation in Dynamo.

	Round 1	Round 2	Round 3	Round 4
Iterations	1	1	1	1
References	1	1	1	1
Cone aperture [°]	120	30	10	2
Cone Sampling [°]	30	10	2	0.5
Azymuth rotation range [°]	360	90	30	5
Azymuth rotation sampling [°]	90	30	5	1
Refine	2	2	2	2
Refine factor	2	2	2	2
High pass filter [pixel]	2	2	2	2
Low pass filter [pixel]	32	32	32	32
Symmetry	C1 / C3	C1 / C3	C1 / C3	C1 / C3
Particle dimensions	192	192	192	192
Shift limits in X, Y and Z [pixel]	12, 12, 12	6, 6, 6	4, 4, 4	2, 2, 2
Shift limiting way	1	2	2	2
Separation in tomogram	0	0	0	0
Basic MRA	0	0	0	0
Threshold parameter	0.8	0.8	0.8	0.8
Threshold modus	5	5	5	5

An isosurface of the final average of the STA was created using USCF Chimera (Pettersen et al., 2004). The post-fusion structure of HA2 (PDB: 1QU1, Chen et al., 1999) was fitted to the isosurface using the 'Fit in Map' function in USCF Chimera. The number of atoms inside and outside of the isosurface were quantified.

Quantification and statistical analysis

Image acquisition and quantification of ILV in late endosomes (Figure 1R–Y) was done blinded. Unpaired T-test was utilized to analyze the significance of differences in the following figure panels: Figure 1H, 1X, 1Q, 1Y, S1C, S3C, S3D, S3E, S3F. Paired T-test was utilized to analyze the significance of differences in the following figure panels: Figure 5B.

1 **Resources**

REAGENT or RESOURCE	SOURCE	IDENTIFIER
Primary antibodies		
Actin	Merck, Sigma-Aldrich	A5441
Caveolin 1 Polyclonal	ThermoFisher Scientific™	PA1-064
IFITM3 Polyclonal	Proteintech Group Inc.	11714-1-AP
M2	Santa Cruz Biotechnology, Inc.	sc-32238
Secondary antibodies		
Anit-Mouse IgGκ light chain binding protein (m-IgGκ BP)	Santa Cruz Biotechnology, Inc.	sc-516102
Goat anti-Rabbit IgG (H+L) Cross-Adsorbed Secondary Antibody, Alexa Fluor™ 680	ThermoFisher Scientific™, Invitrogen	A21076
Goat anti-Rabbit IgG (H+L) Highly Cross-Adsorbed Secondary Antibody, Alexa Fluor™ 633	ThermoFisher Scientific™, Invitrogen	A21071
Mouse anti-Rabbit IgG-HRP	Santa Cruz Biotechnology, Inc.	sc-2357
Bacterial and virus strains		
A/WSN/1933(H1N1)	Hoffmann et al., 2000	N/A
A/WSN/1933(H1N1)-PA-mScarlet	This publication	N/A
E. coli Stellar™ Competent Cells	Takara Bio Inc.	636763
Chemicals, peptides, and recombinant proteins		
1-Hexadecen	Merck, Sigma-Aldrich	822064
Avicel	FMC Corporation	RC-581
Benzonase® Nuclease HC	Merck, Millipore	71206-25KUN
Biotin Azide	ThermoFisher Scientific™	B10184
Bovine Serum Albumin (BSA)	Merck, Sigma-Aldrich	A7030
CellBrite® Green Cytoplasmic Membrane Dye	Biotium	30021
Color Prestained Protein Standard, Broad Range (10-250 kDa)	New England Biolabs	P7719
Color Prestained Protein Standard, Broad Range (11–245 kDa)	New England Biolabs	P7712S
cOmplete™, Mini, EDTA-free Protease Inhibitor Cocktail	ThermoFisher Scientific™, Roche	4693159001
Crystal violet solution, 1%, aqueous solution	Merck, Sigma-Aldrich	V5265
$CuSO_4$	Merck, Sigma-Aldrich	203165
CutSmart® Buffer	New England Biolabs	B7204
DAPI	Merck. Sigma-Aldrich	D9542
DMEM	ThermoFisher Scientific™, Gibco	11965092
DMEM, high glucose, GlutaMAX™	ThermoFisher Scientific™, Gibco	61965026
DMEM/F12	ThermoFisher Scientific™, Gibco	11320033
DMSO	Merck, Sigma-Aldrich	D2650
Fetal bovine serum (FBS)	ThermoFisher Scientific™, Gibco	10270-106
Fish skin gelatine (FSG)	Merck, Sigma-Aldrich	G7765
Glutaraldehyde	Merck, Sigma-Aldrich	G5882

Glycine	ThermoFisher Scientific™	10070150
HEPES	Carl Roth GmbH + Co. KG	9105.2
Hoechst 33342	Merck, Sigma-Aldrich	B2261
Interferon beta (IFNβ)	ImmunoTools GmbH	11343524
Laemmli Sample Buffer (4x)	Bio-Rad Laboratories, Inc.	1610747
Bacto™ Yeast Extraxt (LB)	ThermoFisher Scientific™, Gibco	212750
Lowicryl® HM20 Non-polar, Hydrophobic, -70ºC Embedding Kit	Polysciences Inc.	15924-1
Methanol	Honeywell	32213
Opti-MEM medium	ThermoFisher Scientific™, Gibcon	31985062
Formaldehyde 37% (PFA)	Bernd Kraft GmbH	BK19916
Sylgard 184	Dow Corning Inc.	1673921
PBS	Merck, Sigma-Aldrich	D8537
Penicillin-Streptomycin (P/S) (10.000 units/ml)	ThermoFisher Scientific™	15140122
Photo-reactive clickable trans-Sterol probe (pacChol)	Merck, Sigma-Aldrich	804657
Pierce™ High Capacity NeutrAvidin™ Agarose	ThermoFisher Scientific™	29202
Polybrene infection reagent	Merck, Sigma-Aldrich	TR-1003-G
Polyethylenimine (PEI)	Polysciences	23966-1
ProLong™ Glass Antifade Mountant	ThermoFisher Scientific™, Invitrogen™	P36982
Protease inhibitor cocktail	Roche	11873580001
Protein-A gold 10 nm	Aurion	PA-80830/1
Puromycin	Merck, Sigma-Aldrich	P8833
Recombinant Human Interferon-β 1α	ImmunoTools	11343520
Restriction Endonuclease BssHII	New England Biolabs	R0199S
Restriction Endonuclease XbaI	New England Biolabs	R0145S
S.O.C. medium	ThermoFisher Scientific™, Invitrogen™	15544034
SDS	Serva	20765.03
Sodium deoxycolate	D6750-25G	D6750
TBTA	Merck, Sigma-Aldrich	C4706
TCEP	Merck, Sigma-Aldrich	678937
TGS buffer (10x)	Bio-Rad	1610772
Trypsin from bovine pancreas, TPCK-treated	Merck, Sigma-Aldrich	T1426
Trans-Blot Turbo Mini 0.2 µm PVDF Transfer Packs	Bio-Rad	1704156
TransIT®-2020 Transfection Reagent	Mirus Bio	MIR 5400
TransIT®-293 Transfection Reagent	Mirus Bio	MIR 2700
TransIT®-LT1 Transfection Reagent	Mirus Bio	MIR 2300
Triton™ X-100	Merck, Sigma-Aldrich	X100
Trypsin inhibitor from Glycine max (soybean)	Merck, Sigma-Aldrich	T9128
Tween® 20	Carl Roth GmbH + Co. KG	9127.1

Precision Plus Protein™ All Blue Prestained Protein Standards by Bio-Rad	Bio-Rad	1610373
Uranyl acetate	SERVA Electrophoresis GmbH	77870
Critical commercial assays		
In-fusion® HD Cloning Kit	Takara Bio Inc.	639649
CloneAmp™ HiFi PCR Premix	Takara Bio Inc.	638500
Cloning Enhancer	Takara Bio Inc.	639615
Gateway™ LR Clonase™ Enzyme Mix	ThermoFisher Scientific, Invitrogen™	11791019
Tricine gel	ThermoFisher Scientific	EC66252BOX
NucleoSpin Gel and PCR Clean-up Kit	MACHEREY-NAGEL	740609.50
QIAprep Spin Miniprep Kit	QIAGEN	27104
Beta-Lactamase Loading Solutions Kit	ThermoFisher Scientific, Invitrogen™	K1085
LiveBLAzer™ FRET B/G (CCF4-AM)	ThermoFisher Scientific, Invitrogen™	K1089
Pierce™ BCA Protein Assay Kit	ThermoFisher Scientific	23227
QIAGEN Plasmid Maxi Kit	QIAGEN	12163
Lenti-X™ GoStix	Takara Bio Inc.	631280
Deposited data		
MD simulation data	doi.org/10.5281/zenodo.6599836	N/A
In-situ cryo-ET data	EMD-15130, EMD-15131, EMD-15132, EMD-15133	N/A
HPF/FS ET data	EMD-15705, EMD-15707, EMD-15708	
Fluorescence microscopy data	S-BIAD539	
Immunoblot data	S-BIAD539	
MATLAB code for membrane modeling	https://github.com/GonenGolani/Fusion_Solver	N/A
Experimental models: Cell lines		
A549	American Type Culture Collection (ATCC)	CCL-185
A549-IFITM3	This publication	N/A
HEK293T	American Type Culture Collection (ATCC)	CRL-3216
HEK293T-MCB	Dr. Marco Binder (DKFZ, Heidelberg, Germany)	N/A
MDCK	Prof. João Amorim (Instituto Gulbenkian de Ciência, Portugal)	N/A
Oligonucleotides		
Reverse sequencing primer IRES-rev (TATAGACAAACGCACACCG)	Microsynth	N/A
Forward overhang primer for cloning (CCCACGCCCTGCGCGCGGCAGCAATGGTGTCCAAGGGTGAAGC)	This publication	N/A
Reverse overhang primer for cloning (AAGCAGTTTTCTAGATCACTTGTACAGCTCATCCATTCCAC)	This publication	N/A
Forward primer for sequencing (GGCAAACAACAGATGGCTGGCAAC)	This publication	N/A

Reverse primer for sequencing (GTATGCATCTCCACAACTAGAAGG)	This publication	N/A
Recombinant DNA		
pCAGGS-A/Hong Kong/1968-HA	Chlanda et al., 2015	N/A
pCAGGS-A/Singapore/1957-NA	Chlanda et al., 2015	N/A
pCAGGS-M1-Blam	Tscherne et al., 2010	N/A
pENTR221-clone3728-IFITM3	Dr. Marco Binder (DKFZ, Heidelberg, Germany)	N/A
pWPI-IRES-Puro	Dr. Marco Binder (DKFZ, Heidelberg, Germany)	N/A
pWPI-IFITM3	This publication	N/A
pCMV-VSV-G	addgene	8454
psPAX2	addgene	12260
pAdVantage™	Promega	E1711
pHW2000-PB1-WSN	Dr. Ervin Fodor (University of Oxford, UK)	N/A
pHW2000-PB2-WSN	Dr. Ervin Fodor (University of Oxford, UK)	N/A
pHW2000-PA-WSN	Dr. Ervin Fodor (University of Oxford, UK)	N/A
pHW2000-NP-WSN	Dr. Ervin Fodor (University of Oxford, UK)	N/A
pHW2000-NA-WSN	Dr. Ervin Fodor (University of Oxford, UK)	N/A
pHW2000-M-WSN	Dr. Ervin Fodor (University of Oxford, UK)	N/A
pHW2000-NS-WSN	Dr. Ervin Fodor (University of Oxford, UK)	N/A
pHW2000-HA-WSN	Dr. Ervin Fodor (University of Oxford, UK)	N/A
pHW2000-PA-WSN-mScarlet	Andrew Mehle (University of Wisconsin – Madison, USA)	N/A
pcDNA3.4-mScarlet-codon-optimized	This publication	N/A
pHW2000-PA-WSN-mScarlet-codon-optimized	This publication	N/A
Software and algorithms		
GenSmart™ Codon Optimization, Version Beta 1.0	GenScripts	N/A
FIJI	Schindelin et al., 2012	N/A
IMOD	Kremer et al., 1996	N/A
icy	De Chaumont et al., 2012	N/A
dynamo	Castaño-Díez et al., 2012	N/A
LAS X	Leica Microsystems	N/A
MAPS	Schorb and Sieckmann, 2017	N/A
Prism	GraphPad Software	N/A
Imaris	Oxford Instruments	N/A
Post-correlation cryo-CLEM toolbox	Klein et al., 2021a, github.com/Chlanda-Lab/cryoCLEM	N/A
Cryocare	Buchholz et al., 2019	N/A

Amira	ThermoFisher Scientific	N/A
Motioncor2	Zheng et al., 2017	N/A
MATLAB 2020B	MathWorks	N/A
AutoQuant X3	Media Cybernetics, Inc.	N/A
SerialEM	Mastronarde, 2005	N/A
Magellan™	Tecan Trading AG	N/A
Python 3	Van Rossum and Drake, 2009	N/A
VMD	Humphrey et al., 1996	N/A
GROMACS-2021	Abraham et al., 2015	N/A
Instruments		
UV irradiation system	Vilber Lourmat GmbH	BIO-SUN
Sonicator	Bandelin Sonorex	N/A
Ultracentrifuge	Beckman Coulter, Inc.	Optima L-90K
Rotor for Optima L-90K	Beckman Coulter, Inc.	SW32
Ultracentrifuge	Beckman Coulter, Inc.	Optima TLX
Rotor for Optima TLX	Beckman Coulter, Inc.	TLA-120.2
Mini-PROTEAN Tetra Vertical Electrophoresis Cell	BioRad	1658005
Trans-Blot® Turbo™ Transfer System	BioRad	1704150
Azure 400 chemiluminescent imager	Azure Biosystems	Azure 400
Plate reader	Tecan Trading AG	Infinite 200
High pressure freezing system	Leica Microsystems	EM ICE
Freeze substitution system	Leica Microsystems	EM AFS2
Sputter coater	Leica Microsystems	EM ACE600
Ultramicrotome	Leica Microsystems	EM UC7
Diamond knife for ultramicrotome, 35° angle	DiATOME	DU3520
Consumables		
14 ml round bottom tube	Greiner Bio-One	187261
0.45 µm CME filter	Carl Roth GmbH + Co. KG	KH55.1
Microscopy cover slip NO. 1	Paul Marienfeld GmbH & Co. KG	0111520
Microscopy slides, 76 × 26 mm	Diagonal GmbH & Co. KG	ISO NORM 8037/1
96 well assay plate, black, clear bottom	Corning Incorporated	3603
Sapphire discs for HPF/FS, Ø 3 × 0.05 mm	Leica Microsystems	16702766
Quantifoil EM grid, 200 mesh gold, R1/4 SiO_2 film	Plano GmbH, Germany	S211R14A20 0
EM slot grids 2x1 mm, cupper	Gilder	G2010-Cu
Cloning cylinder, glass, 150 µl	Merck, Sigma-Aldrich	C1059-1EA
Fluorescent microscopes		
SP8 with 63×/1.4 NA HC PL APO CS2 oil immersion objective	Leica Microsystems	N/A
CellDiscoverer 7 with 20×/0.95 NA plan-apochromat air objective	Zeiss	N/A

Eclipse Ts2-FL fluorescent microscope equipped with DS-Fi3 camera	Nikon	TS2-FL DS-Fi3
Objective for Nikon Eclipse Ts2: CFI Achro LWD ADL 20XF (20× / 0.4 NA)	Nikon	MRP46202
Blam-assay filterset for Nikon Eclipse Ts2 (ET Bandpass 395/25, ET dualband beamsplitter DAPI/FITC, ET dualband emitter DAPI/FITC)	Chroma Technology Corporation	ET395/25x 59001bs 59001m
CryoCLEM with 60x/0.9 NA objective	Leica Microsystems	N/A
Electron microscopes		
Cryo-TEM Titan Krios, Gatan K3 camera, GIF	ThermoFisher Scientific	N/A
Cryo-FIB/SEM Acquilos	ThermoFisher Scientific	N/A
TEM Tecnai F30, Gatan OneView 4K camera	FEI	N/A

REFERENCES

Abraham, M.J., Murtola, T., Schulz, R., Páll, S., Smith, J.C., Hess, B., and Lindahl, E. (2015). GROMACS: High performance molecular simulations through multi-level parallelism from laptops to supercomputers. SoftwareX *1–2*, 19–25. https://doi.org/10.1016/j.softx.2015.06.001.

Akimov, S.A., Volynsky, P.E., Galimzyanov, T.R., Kuzmin, P.I., Pavlov, K. V., and Batishchev, O. V. (2017). Pore formation in lipid membrane I: Continuous reversible trajectory from intact bilayer through hydrophobic defect to transversal pore. Sci. Rep. *7*, 1–20. https://doi.org/10.1038/s41598-017-12127-7.

Akimov, S.A., Molotkovsky, R.J., Kuzmin, P.I., Galimzyanov, T.R., and Batishchev, O. V. (2020). Continuum models of membrane fusion: Evolution of the theory. Int. J. Mol. Sci. *21*, 1–36. https://doi.org/10.3390/ijms21113875.

Amini-Bavil-Olyaee, S., Choi, Y.J., Lee, J.H., Shi, M., Huang, I.C., Farzan, M., and Jung, J.U. (2013). The antiviral effector IFITM3 disrupts intracellular cholesterol homeostasis to block viral entry. Cell Host Microbe *13*, 452–464. https://doi.org/10.1016/j.chom.2013.03.006.

Benton, D.J., Nans, A., Calder, L.J., Turner, J., Neu, U., Lin, Y.P., Ketelaars, E., Kallewaard, N.L., Corti, D., Lanzavecchia, A., et al. (2018). Influenza hemagglutinin membrane anchor. Proc. Natl. Acad. Sci. U. S. A. *115*, 10112–10117. https://doi.org/10.1073/pnas.1810927115.

Benton, D.J., Gamblin, S.J., Rosenthal, P.B., and Skehel, J.J. (2020). Structural transitions in influenza haemagglutinin at membrane fusion pH. Nature *583*, 150–153. https://doi.org/10.1038/s41586-020-2333-6.

Bindels, D.S., Haarbosch, L., Van Weeren, L., Postma, M., Wiese, K.E., Mastop, M., Aumonier, S., Gotthard, G., Royant, A., Hink, M.A., et al. (2016). MScarlet: A bright monomeric red fluorescent protein for cellular imaging. Nat. Methods *14*, 53–56. https://doi.org/10.1038/nmeth.4074.

Le Blanc, I., Luyet, P.P., Pons, V., Ferguson, C., Emans, N., Petiot, A., Mayran, N., Demaurex, N., Fauré, J., Sadoul, R., et al. (2005). Endosome-to-cytosol transport of viral nucleocapsids. Nat. Cell Biol. *7*, 653–664. https://doi.org/10.1038/ncb1269.

Brass, A.L., Huang, I.C., Benita, Y., John, S.P., Krishnan, M.N., Feeley, E.M., Ryan, B.J., Weyer, J.L., van der Weyden, L., Fikrig, E., et al. (2009). The IFITM Proteins Mediate Cellular Resistance to Influenza A H1N1 Virus, West Nile Virus, and Dengue Virus. Cell *139*, 1243–1254. https://doi.org/10.1016/j.cell.2009.12.017.

Buchholz, T.-O., Krull, A., Shahidi, R., Pigino, G., Jékely, G., and Jug, F. (2019). Content-aware image restoration for electron microscopy. Methods Cell Biol. *152*, 277–289. https://doi.org/10.1016/bs.mcb.2019.05.001.

Bullough, P.A., Hughson, F.M., Skehel, J.J., and Wiley, D.C. (1994). Structure of influenza haemagglutinin at the pH of membrane fusion. Nature *371*, 37–43. https://doi.org/10.1038/371037a0.

Castaño-Díez, D., Kudryashev, M., Arheit, M., and Stahlberg, H. (2012). Dynamo: A flexible, user-friendly development tool for subtomogram averaging of cryo-EM data in high-performance computing environments. J. Struct. Biol. *178*, 139–151. https://doi.org/10.1016/j.jsb.2011.12.017.

Chanturiya, A., Chernomordik, L. V., and Zimmerberg, J. (1997). Flickering fusion pores comparable with initial exocytotic pores occur in protein-free phospholipid bilayers. Proc. Natl. Acad. Sci. U. S. A. *94*, 14423–14428. https://doi.org/10.1073/pnas.94.26.14423.

De Chaumont, F., Dallongeville, S., Chenouard, N., Hervé, N., Pop, S., Provoost, T., Meas-Yedid, V., Pankajakshan, P., Lecomte, T., Le Montagner, Y., et al. (2012). Icy: An open bioimage informatics platform for extended reproducible research. Nat. Methods *9*, 690–696. https://doi.org/10.1038/nmeth.2075.

Chen, J., Skehel, J.J., and Wiley, D.C. (1999). N- and C-terminal residues combine in the fusion-pH influenza hemagglutinin HA2 subunit to form an N cap that terminates the triple-stranded coiled coil. Proc. Natl. Acad. Sci. U. S. A. *96*, 8967–8972. https://doi.org/10.1073/pnas.96.16.8967.

Chernomordik, L.V., and Kozlov, M.M. (2003). Protein-lipid interplay in fusion and fission of biological membranes. Annu. Rev. Biochem. *72*, 175–207. https://doi.org/10.1146/annurev.biochem.72.121801.161504.

Chernomordik, L., Chanturiya, A., Green, J., and Zimmerberg, J. (1995). The hemifusion intermediate and its conversion to complete fusion: regulation by membrane composition. Biophys. J. *69*, 922–929. https://doi.org/10.1016/S0006-3495(95)79966-0.

Chernomordik, L. V., Kozlov, M.M., Melikyan, G.B., Abidor, I.G., Markin, V.S., and Chizmadzhev, Y.A. (1985). The shape of lipid molecules and monolayer membrane fusion. BBA - Biomembr. *812*, 643–655. https://doi.org/10.1016/0005-2736(85)90257-3.

Chernomordik, L. V., Zimmerberg, J., and Kozlov, M.M. (2006). Membranes of the world unite! J. Cell Biol. *175*, 201–207. https://doi.org/10.1083/jcb.200607083.

Chesarino, N.M., Compton, A.A., McMichael, T.M., Kenney, A.D., Zhang, L., Soewarna, V., Davis, M., Schwartz, O., and Yount, J.S. (2017). IFITM 3 requires an amphipathic helix for antiviral activity. EMBO Rep. *18*, 1740–1751. https://doi.org/10.15252/embr.201744100.

Chlanda, P., Schraidt, O., Kummer, S., Riches, J., Oberwinkler, H., Prinz, S., Kräusslich, H.-G., and Briggs, J.A.G. (2015). Structural Analysis of the Roles of Influenza A Virus Membrane-Associated Proteins in Assembly and Morphology. J. Virol. *89*, 8957–8966. https://doi.org/10.1128/jvi.00592-15.

Chlanda, P., Mekhedov, E., Waters, H., Schwartz, C.L., Fischer, E.R., Ryham, R.J., Cohen, F.S., Blank, P.S., and Zimmerberg, J. (2016). The hemifusion structure induced by influenza virus haemagglutinin is determined by physical properties of the target membranes. Nat. Microbiol. *1*, 1–8. https://doi.org/10.1038/nmicrobiol.2016.50.

Chmielewska, A.M., Gómez-Herranz, M., Gach, P., Nekulova, M., Bagnucka, M.A., Lipińska, A.D., Rychłowski, M., Hoffmann, W., Król, E., Vojtesek, B., et al. (2022). The Role of IFITM Proteins in Tick-Borne Encephalitis Virus Infection. J. Virol. *96*, e0113021. https://doi.org/10.1128/JVI.01130-21.

Darden, T., York, D., and Pedersen, L. (1993). Particle mesh Ewald: An *N* ·log(*N*) method for Ewald sums in large systems. J. Chem. Phys. *98*, 10089–10092. https://doi.org/10.1063/1.464397.

Das, T., Yang, X., Lee, H., Garst, E., Valencia, E., Chandran, K., Im, W., and Hang, H. (2021). S-palmitoylation and sterol interactions mediate antiviral specificity of IFITM isoforms. PREPRINT (Version 1). Res. Sq. https://doi.org/10.21203/rs.3.rs-1179000/v1.

Desai, T.M., Marin, M., Chin, C.R., Savidis, G., Brass, A.L., and Melikyan, G.B. (2014). IFITM3 Restricts Influenza A Virus Entry by Blocking the Formation of Fusion Pores following Virus-Endosome Hemifusion. PLoS Pathog. *10*, e1004048. https://doi.org/10.1371/journal.ppat.1004048.

Dimova, R. (2014). Recent developments in the field of bending rigidity measurements on membranes. Adv. Colloid Interface Sci. *208*, 225–234. https://doi.org/10.1016/j.cis.2014.03.003.

Doktorova, M., Harries, D., and Khelashvili, G. (2017). Determination of bending rigidity and tilt modulus of lipid membranes from real-space fluctuation analysis of molecular dynamics simulations. Phys. Chem. Chem. Phys. *19*, 16806–16818. https://doi.org/10.1039/c7cp01921a.

Dou, D., Revol, R., Östbye, H., Wang, H., and Daniels, R. (2018). Influenza A virus cell entry, replication, virion assembly and movement. Front. Immunol. *9*, 1581. https://doi.org/10.3389/fimmu.2018.01581.

Essmann, U., Perera, L., Berkowitz, M.L., Darden, T., Lee, H., and Pedersen, L.G. (1995). A smooth particle mesh Ewald method. J. Chem. Phys. *103*, 8577–8593. https://doi.org/10.1063/1.470117.

Feeley, E.M., Sims, J.S., John, S.P., Chin, C.R., Pertel, T., Chen, L.M., Gaiha, G.D., Ryan, B.J., Donis, R.O., Elledge, S.J., et al. (2011). IFITM3 inhibits influenza a virus infection by preventing cytosolic entry. PLoS Pathog. *7*, e1002337. https://doi.org/10.1371/journal.ppat.1002337.

Fontana, J., Cardone, G., Heymann, J.B., Winkler, D.C., and Steven, A.C. (2012). Structural Changes in Influenza Virus at Low pH Characterized by Cryo-Electron Tomography. J. Virol. *86*, 2919–2929. https://doi.org/10.1128/jvi.06698-11.

Frolov, V.A., Cho, M.S., Bronk, P., Reese, T.S., and Zimmerberg, J. (2000). Multiple local contact sites are induced by GPI-linked influenza hemagglutinin during hemifusion and flickering pore formation. Traffic Cph. Den. *1*, 622–630. https://doi.org/10.1034/j.1600-0854.2000.010806.x.

Fuhrmans, M., Marelli, G., Smirnova, Y.G., and Müller, M. (2015). Mechanics of membrane fusion/pore formation. Chem. Phys. Lipids *185*, 109–128. https://doi.org/10.1016/j.chemphyslip.2014.07.010.

Fuller, N., and Rand, R.P. (2001). The influence of lysolipids on the spontaneous curvature and bending elasticity of phospholipid membranes. Biophys. J. *81*, 243–254. https://doi.org/10.1016/S0006-3495(01)75695-0.

Garst, E.H., Lee, H., Das, T., Bhattacharya, S., Percher, A., Wiewiora, R., Witte, I.P., Li, Y., Peng, T., Im, W., et al. (2021). Site-Specific Lipidation Enhances IFITM3 Membrane Interactions and Antiviral Activity. ACS Chem. Biol. *16*, 844–856. https://doi.org/10.1021/acschembio.1c00013.

Giard, D.J., Aaronson, S.A., Todaro, G.J., Arnstein, P., Kersey, J.H., Dosik, H., and Parks, W.P. (1973). In vitro cultivation of human tumors: Establishment of cell lines derived from a series of solid tumors. J. Natl. Cancer Inst. *51*, 1417–1423. https://doi.org/10.1093/jnci/51.5.1417.

Golani, G., Leikina, E., Melikov, K., Whitlock, J.M., Gamage, D.G., Luoma-Overstreet, G., Millay, D.P., Kozlov, M.M., and Chernomordik, L. V. (2021). Myomerger promotes fusion pore by elastic coupling between proximal membrane leaflets and hemifusion diaphragm. Nat. Commun. *12*, 1–18. https://doi.org/10.1038/s41467-020-20804-x.

Guo, X., Steinkühler, J., Marin, M., Li, X., Lu, W., Dimova, R., and Melikyan, G.B. (2021). Interferon-induced transmembrane protein 3 blocks fusion of diverse enveloped viruses by altering mechanical properties of cell membranes. ACS Nano *15*, 8155–8170. https://doi.org/10.1021/acsnano.0c10567.

Hagen, W.J.H., Wan, W., and Briggs, J.A.G. (2017). Implementation of a cryo-electron tomography tilt-scheme optimized for high resolution subtomogram averaging. J. Struct. Biol. *197*, 191–198. https://doi.org/10.1016/j.jsb.2016.06.007.

Hamm, M., and Kozlov, M.M. (1998). Tilt model of inverted amphiphilic mesophases. Eur. Phys. J. B *6*, 519–528. https://doi.org/10.1007/s100510050579.

Hamm, M., and Kozlov, M.M. (2000). Elastic energy of tilt and bending of fluid membranes. Eur. Phys. J. E *3*, 323–335. https://doi.org/10.1007/s101890070003.

Harrison, S.C. (2008). Viral membrane fusion. Nat. Struct. Mol. Biol. *15*, 690–698. https://doi.org/10.1038/nsmb.1456.

Hastings, K.T., and Cresswell, P. (2011). Disulfide Reduction in the Endocytic Pathway: Immunological Functions of Gamma-Interferon-Inducible Lysosomal Thiol Reductase. Antioxid. Redox Signal. *15*, 657–668. https://doi.org/10.1089/ars.2010.3684.

Helfrich, W. (1973). Elastic properties of lipid bilayers: theory and possible experiments. Z. Naturforschung Teil C Biochem. Biophys. Biol. Virol. *28*, 693–703. https://doi.org/10.1515/znc-1973-11-1209.

Hess, B., Bekker, H., Berendsen, H.J.C., and Fraaije, J.G.E.M. (1997). LINCS: A linear constraint solver for molecular simulations. J. Comput. Chem. *18*, 1463–1472. https://doi.org/10.1002/(SICI)1096-987X(199709)18:12<1463::AID-JCC4>3.0.CO;2-H.

Hoffmann, E., Neumann, G., Kawaoka, Y., Hobom, G., and Webster, R.G. (2000). A DNA transfection system for generation of influenza A virus from eight plasmids. Proc. Natl. Acad. Sci. U. S. A. *97*, 6108–6113. https://doi.org/10.1073/pnas.100133697.

Hoover, W.G. (1985). Canonical dynamics: Equilibrium phase-space distributions. Phys. Rev. A *31*, 1695–1697. https://doi.org/10.1103/PhysRevA.31.1695.

Huang, J., and MacKerell, A.D. (2013). CHARMM36 all-atom additive protein force field: validation based on comparison to NMR data. J. Comput. Chem. *34*, 2135–2145. https://doi.org/10.1002/jcc.23354.

Huang, I.-C., Bailey, C.C., Weyer, J.L., Radoshitzky, S.R., Becker, M.M., Chiang, J.J., Brass, A.L., Ahmed, A.A., Chi, X., Dong, L., et al. (2011). Distinct patterns of IFITM-mediated restriction of filoviruses, SARS coronavirus, and influenza A virus. PLoS Pathog. *7*, e1001258. https://doi.org/10.1371/journal.ppat.1001258.

Huang, J., Rauscher, S., Nawrocki, G., Ran, T., Feig, M., de Groot, B.L., Grubmüller, H., and MacKerell, A.D. (2017). CHARMM36m: an improved force field for folded and intrinsically disordered proteins. Nat. Methods *14*, 71–73. https://doi.org/10.1038/nmeth.4067.

Humphrey, W., Dalke, A., and Schulten, K. (1996). VMD: Visual molecular dynamics. J. Mol. Graph. *14*, 33–38. https://doi.org/10.1016/0263-7855(96)00018-5.

Huotari, J., and Helenius, A. (2011). Endosome maturation. EMBO J. *30*, 3481–3500. https://doi.org/10.1038/emboj.2011.286.

Jones, D.M., and Padilla-Parra, S. (2016). The β-lactamase assay: Harnessing a FRET biosensor to analyse viral fusion mechanisms. Sens. Switz. *16*. https://doi.org/10.3390/s16070950.

Jorgensen, W.L., Chandrasekhar, J., Madura, J.D., Impey, R.W., and Klein, M.L. (1983). Comparison of simple potential functions for simulating liquid water. J. Chem. Phys. *79*, 926–935. https://doi.org/10.1063/1.445869.

Kasson, P.M., and Pande, V.S. (2007). Control of membrane fusion mechanism by lipid composition: Predictions from ensemble molecular dynamics. PLoS Comput. Biol. *3*, 2228–2238. https://doi.org/10.1371/journal.pcbi.0030220.

Kemble, G.W., Danieli, T., and White, J.M. (1994). Lipid-anchored influenza hemagglutinin promotes hemifusion, not complete fusion. Cell *76*, 383–391. https://doi.org/10.1016/0092-8674(94)90344-1.

Klein, S., Wachsmuth-Melm, M., Winter, S.L., Kolovou, A., and Chlanda, P. (2021a). Cryo-correlative light and electron microscopy workflow for cryo-focused ion beam milled adherent cells. Methods Cell Biol. *162*, 273–302. https://doi.org/10.1016/bs.mcb.2020.12.009.

Klein, S., Wimmer, B.H., Winter, S.L., Kolovou, A., Laketa, V., and Chlanda, P. (2021b). Post-correlation on-lamella cryo-CLEM reveals the membrane architecture of lamellar bodies. Commun. Biol. *4*, 1–12. https://doi.org/10.1038/s42003-020-01567-z.

Kobayashi, T., Beuchat, M.H., Chevallier, J., Makino, A., Mayran, N., Escola, J.M., Lebrand, C., Cosson, P., Kobayashi, T., and Gruenberg, J. (2002). Separation and characterization of late endosomal membrane domains. J. Biol. Chem. *277*, 32157–32164. https://doi.org/10.1074/jbc.M202838200.

Kollmitzer, B., Heftberger, P., Rappolt, M., and Pabst, G. (2013). Monolayer spontaneous curvature of raft-forming membrane lipids. Soft Matter *9*, 10877–10884. https://doi.org/10.1039/c3sm51829a.

Kozlov, M.M., and Helfrich, W. (1992). Effects of a Cosurfactant on the Stretching and Bending Elasticities of a Surfactant Monolayer. Langmuir *8*, 2792–2797. https://doi.org/10.1021/la00047a035.

Kozlov, M.M., and Winterhalter, M. (1991). Elastic moduli for strongly curved monoplayers. Position of the neutral surface. J. Phys. II *1*, 1077–1084. https://doi.org/10.1051/jp2:1991201.

Kozlovsky, Y., Chernomordik, L. V., and Kozlov, M.M. (2002). Lipid intermediates in membrane fusion: Formation, structure, and decay of hemifusion diaphragm. Biophys. J. *83*, 2634–2651. https://doi.org/10.1016/S0006-3495(02)75274-0.

Kremer, J.R., Mastronarde, D.N., and McIntosh, J.R. (1996). Computer visualization of three-dimensional image data using IMOD. J. Struct. Biol. *116*, 71–76. https://doi.org/10.1006/jsbi.1996.0013.

Kühnl, A., Musiol, A., Heitzig, N., Johnson, D.E., Ehrhardt, C., Grewal, T., Gerke, V., Ludwig, S., and Rescher, U. (2018). Late endosomal/lysosomal cholesterol accumulation is a host cell-protective mechanism inhibiting endosomal escape of influenza A virus. MBio *9*. https://doi.org/10.1128/mBio.01345-18.

Kumar, V., Butcher, S.J., Öörni, K., Engelhardt, P., Heikkonen, J., Kaski, K., Ala-Korpela, M., and Kovanen, P.T. (2011). Three-dimensional cryoEM reconstruction of native LDL particles to 16å resolution at physiological body temperature. PLoS ONE *6*, e18841. https://doi.org/10.1371/journal.pone.0018841.

Lawson, C.L., Patwardhan, A., Baker, M.L., Hryc, C., Garcia, E.S., Hudson, B.P., Lagerstedt, I., Ludtke, S.J., Pintilie, G., Sala, R., et al. (2016). EMDataBank unified data resource for 3DEM. Nucleic Acids Res. *44*, D396-403. https://doi.org/10.1093/nar/gkv1126.

Lee, K.K. (2010). Architecture of a nascent viral fusion pore. EMBO J. *29*, 1299–1311. https://doi.org/10.1038/emboj.2010.13.

Lee, J., Cheng, X., Swails, J.M., Yeom, M.S., Eastman, P.K., Lemkul, J.A., Wei, S., Buckner, J., Jeong, J.C., Qi, Y., et al. (2016). CHARMM-GUI Input Generator for NAMD, GROMACS, AMBER, OpenMM, and CHARMM/OpenMM Simulations Using the CHARMM36 Additive Force Field. J. Chem. Theory Comput. *12*, 405–413. https://doi.org/10.1021/acs.jctc.5b00935.

Lee, J., Patel, D.S., Ståhle, J., Park, S.-J., Kern, N.R., Kim, S., Lee, J., Cheng, X., Valvano, M.A., Holst, O., et al. (2019). CHARMM-GUI Membrane Builder for Complex Biological Membrane Simulations with Glycolipids and Lipoglycans. J. Chem. Theory Comput. *15*, 775–786. https://doi.org/10.1021/acs.jctc.8b01066.

Ling, S., Zhang, C., Wang, W., Cai, X., Yu, L., Wu, F., Zhang, L., and Tian, C. (2016). Combined approaches of EPR and NMR illustrate only one transmembrane helix in the human IFITM3. Sci. Rep. *6*, 1–8. https://doi.org/10.1038/srep24029.

Lorent, J.H., Levental, K.R., Ganesan, L., Rivera-Longsworth, G., Sezgin, E., Doktorova, M., Lyman, E., and Levental, I. (2020). Plasma membranes are asymmetric in lipid unsaturation, packing and protein shape. Nat. Chem. Biol. *16*, 644–652. https://doi.org/10.1038/s41589-020-0529-6.

de Marco, M.C., Kremer, L., Albar, J.P., Martinez-Menarguez, J.A., Ballesta, J., Garcia-Lopez, M.A., Marazuela, M., Puertollano, R., and Alonso, M.A. (2001). BENE, a novel raft-associated protein of the MAL proteolipid family, interacts with caveolin-1 in human endothelial-like ECV304 cells. J. Biol. Chem. *276*, 23009–23017. https://doi.org/10.1074/jbc.M009739200.

Marko, M., Hsieh, C., Schalek, R., Frank, J., and Mannella, C. (2007). Focused-ion-beam thinning of frozen-hydrated biological specimens for cryo-electron microscopy. Nat. Methods *4*, 215–217. https://doi.org/10.1038/nmeth1014.

Mastronarde, D.N. (2005). Automated electron microscope tomography using robust prediction of specimen movements. J. Struct. Biol. *152*, 36–51. https://doi.org/10.1016/j.jsb.2005.07.007.

Matlin, K.S., Reggio, H., Helenius, A., and Simons, K. (1981). Infectious entry pathway of influenza virus in a canine kidney cell line. J. Cell Biol. *91*, 601–613. https://doi.org/10.1083/jcb.91.3.601.

May, S., Kozlovsky, Y., Ben-Shaul, A., and Kozlov, M.M. (2004). Tilt modulus of a lipid monolayer. Eur. Phys. J. E *14*, 299–308. https://doi.org/10.1140/epje/i2004-10019-y.

Van Meer, G., Voelker, D.R., and Feigenson, G.W. (2008). Membrane lipids: Where they are and how they behave. Nat. Rev. Mol. Cell Biol. *9*, 112–124. https://doi.org/10.1038/nrm2330.

Nosé, S. (1984). A molecular dynamics method for simulations in the canonical ensemble. Mol. Phys. *52*, 255–268. https://doi.org/10.1080/00268978400101201.

Odon, V., Fros, J.J., Goonawardane, N., Dietrich, I., Ibrahim, A., Alshaikhahmed, K., Nguyen, D., and Simmonds, P. (2019). The role of ZAP and OAS3/RNAseL pathways in the attenuation of an RNA virus with elevated frequencies of CpG and UpA dinucleotides. Nucleic Acids Res. *47*, 8061–8083. https://doi.org/10.1093/nar/gkz581.

Parrinello, M., and Rahman, A. (1981). Polymorphic transitions in single crystals: A new molecular dynamics method. J. Appl. Phys. *52*, 7182–7190. https://doi.org/10.1063/1.328693.

Pastor, R.W., and Mackerell, A.D. (2011). Development of the CHARMM Force Field for Lipids. J. Phys. Chem. Lett. *2*, 1526–1532. https://doi.org/10.1021/jz200167q.

Perrin, P., Janssen, L., Janssen, H., van den Broek, B., Voortman, L.M., van Elsland, D., Berlin, I., and Neefjes, J. (2021). Retrofusion of intralumenal MVB membranes parallels viral infection and coexists with exosome release. Curr. Biol. *31*, 3884-3893.e4. https://doi.org/10.1016/j.cub.2021.06.022.

Pettersen, E.F., Goddard, T.D., Huang, C.C., Couch, G.S., Greenblatt, D.M., Meng, E.C., and Ferrin, T.E. (2004). UCSF Chimera - A visualization system for exploratory research and analysis. J. Comput. Chem. *25*, 1605–1612. https://doi.org/10.1002/jcc.20084.

Portet, T., and Dimova, R. (2010). A new method for measuring edge tensions and stability of lipid bilayers: Effect of membrane composition. Biophys. J. *99*, 3264–3273. https://doi.org/10.1016/j.bpj.2010.09.032.

Rigort, A., Bäuerlein, F.J.B., Villa, E., Eibauer, M., Laugks, T., Baumeister, W., and Plitzko, J.M. (2012). Focused ion beam micromachining of eukaryotic cells for cryoelectron tomography. Proc. Natl. Acad. Sci. U. S. A. *109*, 4449–4454. https://doi.org/10.1073/pnas.1201333109.

Risselada, H.J., and Grubmüller, H. (2021). How proteins open fusion pores: insights from molecular simulations. Eur. Biophys. J. *50*, 279–293. https://doi.org/10.1007/s00249-020-01484-3.

Safran, S.A., Pincus, P., and Andelman, D. (1990). Theory of spontaneous vesicle formation in surfactant mixtures. Science *248*, 354–356. https://doi.org/10.1126/science.248.4953.354.

Sarkans, U., Gostev, M., Athar, A., Behrangi, E., Melnichuk, O., Ali, A., Minguet, J., Rada, J.C., Snow, C., Tikhonov, A., et al. (2018). The BioStudies database—one stop shop for all data supporting a life sciences study. Nucleic Acids Res. *46*, D1266–D1270. https://doi.org/10.1093/nar/gkx965.

Schindelin, J., Arganda-Carreras, I., Frise, E., Kaynig, V., Longair, M., Pietzsch, T., Preibisch, S., Rueden, C., Saalfeld, S., Schmid, B., et al. (2012). Fiji: An open-source platform for biological-image analysis. Nat. Methods *9*, 676–682. https://doi.org/10.1038/nmeth.2019.

Schmidt, U., Weigert, M., Broaddus, C., and Myers, G. (2018). Cell Detection with Star-Convex Polygons. Lect. Notes Comput. Sci. *11071 LNCS*, 265–273. https://doi.org/10.1007/978-3-030-00934-2_30.

Schorb, M., and Sieckmann, F. (2017). Matrix MAPS-an intuitive software to acquire, analyze, and annotate light microscopy data for CLEM. Methods Cell Biol. *140*, 321–333. https://doi.org/10.1016/bs.mcb.2017.03.012.

Schorb, M., Gaechter, L., Avinoam, O., Sieckmann, F., Clarke, M., Bebeacua, C., Bykov, Y.S., Sonnen, A.F.-P., Lihl, R., and Briggs, J.A.G. (2017). New hardware and workflows for semi-automated correlative cryo-fluorescence and cryo-electron microscopy/tomography. J. Struct. Biol. *197*, 83–93. https://doi.org/10.1016/j.jsb.2016.06.020.

Skehel, J.J., Bayley, P.M., Brown, E.B., Martin, S.R., Waterfield, M.D., White, J.M., Wilson, I.A., and Wiley, D.C. (1982). Changes in the conformation of influenza virus hemagglutinin at the pH optimum of virus mediated membrane fusion. Proc. Natl. Acad. Sci. U. S. A. *79*, 968–972. https://doi.org/10.1073/pnas.79.4.968.

Suddala, K.C., Lee, C.C., Meraner, P., Marin, M., Markosyan, R.M., Desai, T.M., Cohen, F.S., Brass, A.L., and Melikyan, G.B. (2019). Interferon-induced transmembrane protein 3 blocks fusion of sensitive but not resistant viruses by partitioning into virus-carrying endosomes. PLoS Pathog. *15*, e1007532. https://doi.org/10.1371/journal.ppat.1007532.

Taupin, C., Dvolaitzky, M., and Sauterey, C. (1975). Osmotic Pressure Induced Pores in Phospholipid Vesicles. Biochemistry *14*, 4771–4775. https://doi.org/10.1021/bi00692a032.

Templer, R.H., Khoo, B.J., and Seddon, J.M. (1998). Gaussian curvature modulus of an amphiphilic monolayer. Langmuir *14*, 7427–7434. https://doi.org/10.1021/la980701y.

Terzi, M.M., and Deserno, M. (2017). Novel tilt-curvature coupling in lipid membranes. J. Chem. Phys. *147*, 084702. https://doi.org/10.1063/1.4990404.

Terzi, M.M., Ergüder, M.F., and Deserno, M. (2019). A consistent quadratic curvature-tilt theory for fluid lipid membranes. J. Chem. Phys. *151*, 164108. https://doi.org/10.1063/1.5119683.

Tran, V., Moser, L.A., Poole, D.S., and Mehle, A. (2013). Highly Sensitive Real-Time In Vivo Imaging of an Influenza Reporter Virus Reveals Dynamics of Replication and Spread. J. Virol. *87*, 13321–13329. https://doi.org/10.1128/jvi.02381-13.

Tscherne, D.M., Manicassamy, B., and García-Sastre, A. (2010). An enzymatic virus-like particle assay for sensitive detection of virus entry. J. Virol. Methods *163*, 336–343. https://doi.org/10.1016/j.jviromet.2009.10.020.

Van Rossum, G., and Drake, F.L. (2009). Python 3 Reference Manual (Scotts Valley, CA: CreateSpace).

de Vries, E., Tscherne, D.M., Wienholts, M.J., Cobos-Jiménez, V., Scholte, F., García-Sastre, A., Rottier, P.J.M., and de Haan, C.A.M. (2011). Dissection of the influenza a virus endocytic routes reveals macropinocytosis as an alternative entry pathway. PLoS Pathog. *7*, e1001329. https://doi.org/10.1371/journal.ppat.1001329.

Wagner, F.R., Watanabe, R., Schampers, R., Singh, D., Persoon, H., Schaffer, M., Fruhstorfer, P., Plitzko, J., and Villa, E. (2020). Preparing samples from whole cells using focused-ion-beam milling for cryo-electron tomography. Nat. Protoc. *15*, 2041–2070. https://doi.org/10.1038/s41596-020-0320-x.

Weaver, J.C., and Chizmadzhev, Y.A. (1996). Theory of electroporation: A review. Bioelectrochem. Bioenerg. *41*, 135–160. https://doi.org/10.1016/S0302-4598(96)05062-3.

Wolff, G., Limpens, R.W.A.L., Zheng, S., Snijder, E.J., Agard, D.A., Koster, A.J., and Bárcena, M. (2019). Mind the gap: Micro-expansion joints drastically decrease the bending of FIB-milled cryo-lamellae. J. Struct. Biol. *208*. https://doi.org/10.1016/j.jsb.2019.09.006.

Yang, S.T., Kreutzberger, A.J.B., Lee, J., Kiessling, V., and Tamm, L.K. (2016). The role of cholesterol in membrane fusion. Chem. Phys. Lipids *199*, 136–143. https://doi.org/10.1016/j.chemphyslip.2016.05.003.

Yount, J.S., Moltedo, B., Yang, Y.Y., Charron, G., Moran, T.M., López, C.B., and Hang, H.C. (2010). Palmitoylome profiling reveals S-palmitoylation-dependent antiviral activity of IFITM3. Nat. Chem. Biol. *6*, 610–614. https://doi.org/10.1038/nchembio.405.

Zambrano, F., Fleischer, S., and Fleischer, B. (1975). Lipid composition of the golgi apparatus of rat kidney and liver in comparison with other subcellular organelles. Biochim. Biophys. Acta BBALipids Lipid Metab. *380*, 357–369. https://doi.org/10.1016/0005-2760(75)90104-6.

Zani, A., and Yount, J.S. (2018). Antiviral Protection by IFITM3 In Vivo. Curr. Clin. Microbiol. Rep. *5*, 229–237. https://doi.org/10.1007/s40588-018-0103-0.

Zheng, S.Q., Palovcak, E., Armache, J.P., Verba, K.A., Cheng, Y., and Agard, D.A. (2017). MotionCor2: Anisotropic correction of beam-induced motion for improved cryo-electron microscopy. Nat. Methods *14*, 331–332. https://doi.org/10.1038/nmeth.4193.